Decomposing pre-industrial to present-day land use change forcing in the UK Earth System Model

Emma Sands[1], Fiona M. O'Connor[2,3], James Weber[4], Ruth M. Doherty[1], and Richard J. Pope[5,6]

[1]School of Geosciences, University of Edinburgh, Edinburgh, United Kingdom
[2]Met Office Hadley Centre, Exeter, United Kingdom
[3]Department of Mathematics and Statistics, Global Systems Institute, University of Exeter, Exeter, United Kingdom
[4]Department of Meteorology, University of Reading, United Kingdom
[5]School of Earth and Environment, University of Leeds, Leeds, United Kingdom
[6]National Centre for Earth Observation, University of Leeds, Leeds, United Kingdom

Correspondence: Emma Sands (e.g.sands@ed.ac.uk)

Abstract. Land use impacts climate through changes in carbon emissions, surface albedo and evapotranspiration, as well as biogenic volatile organic compound (BVOC) emissions, which influence atmospheric composition. The relative importance of changes in atmospheric composition driven by pre-industrial to present-day land use change has not been assessed for the UK Earth System Model (UKESM). Here, we decompose the pre-industrial to present-day land use change forcing in UKESM1.1 with additional process updates. We find a net simulated forcing of -0.08 ± 0.05 W m^{-2} when using the standard (Strat-Trop vn1.0) chemistry, and -0.12 ± 0.04 W m^{-2} for a more complex (CRI-Strat 2) chemical mechanism. The simulated forcing includes the positive aerosol direct and indirect effects (around $+0.06$ W m^{-2} and $+0.085$ W m^{-2}, respectively), alongside negative forcings from ozone (around -0.01 W m^{-2}) and surface albedo change (around -0.17 W m^{-2}). The forcing from the aerosol indirect effects calculated in this study is greater than in recent UKESM BVOC forcing experiments, which we attribute to using pre-industrial background conditions and increased organic matter hygroscopicity. Additional calculations show the radiative forcing from changes to methane lifetime is between -0.02 and -0.04 W m^{-2}, while the land use carbon emissions drive a carbon dioxide forcing of $+0.87$ W m^{-2}. Overall, the competing effects of changes in aerosols and short-lived greenhouse gases with surface albedo counter around 15% of the carbon dioxide forcing. However, non-carbon dioxide effects have significant regional impacts.

1 Introduction

Land use change is the source of around one-third of the total anthropogenic carbon dioxide (CO$_2$) emissions since 1750 (Canadell et al., 2007). Additionally, changes in land cover influence surface albedo, surface roughness and evapotranspiration (Davin et al., 2007; Davin and Noblet-Ducoudré, 2010), while the loss or gain of vegetation affects the emissions of various gases and aerosols (e.g. Ganzeveld et al. (2010); Ito and Hajima (2020); Wu et al. (2012)). Despite recognition that land-use driven changes in atmospheric composition have climate impacts (Fiore et al., 2012; Heald and Spracklen, 2015), only a few studies have attempted to decompose the pre-industrial (PI) to present-day (PD) radiative forcing from changes in land use/land

cover, referred to here as land use, into the various atmospheric chemistry and aerosol pathways (Heald and Geddes, 2016; Scott et al., 2017; Unger, 2014a, b; Ward et al., 2014). Additionally, the continued development of Earth system models (ESMs) results in the inclusion of new and updated process representation that impacts these forcings (e.g. Weber et al. (2022)). This study re-evaluates the PI to PD land use radiative forcing using the United Kingdom Earth System Model vn1.1 (UKESM1.1) with these updated or new processes and parameterisations, focusing on the changes in atmospheric chemistry and aerosols.

There are multiple pathways through which land use change can drive changes in atmospheric composition that have climate impacts. Biogenic volatile organic compounds (BVOCs) are tropospheric ozone (O_3) precursors, while their oxidation reactions can also be O_3 sinks. Consequently, any change in their emission can affect the concentrations of this greenhouse gas, although the sign of the impact will also depend on nitrogen oxide (NO_x) concentrations (Seinfeld and Pandis, 2016). In addition, BVOCs are rapidly oxidised in the troposphere and can, therefore, affect the availability of the hydroxyl radical (OH) for reactions with other gases, resulting in a link between BVOC emissions and the atmospheric oxidation capacity (Wang et al., 2022). Of particular interest for the land use radiative forcing is the potential impact via OH on the methane (CH_4) lifetime. Finally, BVOCs are also secondary organic aerosol (SOA) precursors and, consequently, affect both aerosol-radiation interactions (ARI, also known as the aerosol direct effect) and aerosol-cloud interactions (ACI, or the aerosol indirect effects), thereby influencing climate (e.g. Scott et al. (2014)).

The influence of NO_x on O_3 formation is just one example of how the impacts of changes in BVOC emissions depend on background conditions. The BVOC emission flux is sensitive to atmospheric CO_2, as well as temperature and sunlight (Guenther et al., 1995, 2012; Hantson et al., 2017). The initial availability of oxidants will determine how important a land-use driven change in BVOCs is for, e.g., aerosol formation pathways and methane lifetime. Previous studies have found that PI to PD aerosol forcing calculations are significantly affected by the background aerosol state in the PI (Carslaw et al., 2017; Rap et al., 2013). Further, the geophysical effects of land use change, such as changes in albedo and evapotranspiration, affect the radiative balance and drive rapid adjustments (e.g. changes in surface temperature) that can feedback on biogenic emissions.

Previous research into PI-PD land use radiative forcing from changes in atmospheric composition has used a variety of models and experimental set ups, as well as definitions of radiative forcing, leading to a wide range of results. The effective radiative forcing (ERF) is the change in the top-of-atmosphere net radiative flux (incoming - outgoing) after tropospheric and stratospheric adjustments, while Earth's surface temperature remains fixed. Ideally, both land surface and ocean temperatures would remain fixed. However, due to modelling constraints, land surface temperature adjustments are typically allowed to occur. Alternative metrics include the stratospherically-adjusted radiative forcing (SARF), which focuses on the change in the radiative flux after allowing for stratospheric adjustments but keeping the tropospheric conditions fixed, and the instantaneous radiative forcing (IRF), which does not include any adjustments. For the following discussion of existing literature, we use the introduced radiative forcing terms explicitly when the definition of the forcing is clear in the literature.

Early modelling experiments on BVOC impacts by Unger (2014a, b) suggested that the decrease in BVOC emissions from PI to PD land use change likely had a net negative forcing of $-0.11\pm0.17\,\mathrm{W\,m^{-2}}$ or $-0.17\pm0.01\,\mathrm{W\,m^{-2}}$. The different values were due to using different methodologies and background conditions, including different climate conditions and anthropogenic emissions of gases and aerosols. Climate influences the magnitude of the BVOC emissions, while the presence of other trace

gases, in particular NO_x, and aerosols affects BVOC oxidation and subsequent impacts. The results of the two studies also showed different magnitudes for the O_3, CH_4 and biogenic ARI forcings. Unger (2014a) calculated, using PD atmospheric background conditions, a substantial contribution from O_3 (-0.13 W m^{-2}) compared to CH_4 and ARI from biogenic SOA
60   (-0.06 and $+0.09$ W m^{-2}, respectively). When the impact from other anthropogenic changes was considered (Unger, 2014b), the CH_4 forcing became more prominent (-0.12 W m^{-2}), as it was an order of magnitude greater than the O_3 and biogenic SOA ARI impacts (-0.03 to -0.012 W m^{-2}, respectively). Heald and Spracklen (2015) calculated forcings of similar magnitude from land-use-driven changes in O_3 (-0.11 W m^{-2}) and biogenic SOA ARI ($+0.012$ to $+0.056$ W m^{-2}). Their estimate of the global mean PI to PD radiative effect from land-use-driven changes in atmospheric composition was -0.21 W m^{-2} (range
65   of -0.28 to -0.14 W m^{-2}). Note that ACI were not considered in each of these studies.

The role of ACI in the radiative forcing from land use change became more apparent once organically mediated nucleation was included in models. This process increased the sensitivity of cloud condensation nuclei to SOA (Rap et al., 2013; Scott et al., 2014). Scott et al. (2017) found the ARI and ACI forcings ($IRF_{ARI} = +0.02$ and $RF_{ACI} = +0.008$ W m^{-2}) in combination slightly outweighed the negative O_3 and CH_4 forcings ($ERF_{O3} = -0.02$ and $SARF_{CH4} = -0.007$ W m^{-2}), resulting in a
70   minimal net positive land use change forcing from changes in atmospheric composition. This research highlights the importance of considering both direct and indirect aerosol effects, and the aerosol effects may be even greater under different background conditions. The use of PD atmospheric background conditions in the Scott et al. (2017) study may have decreased the net radiative effect; organic aerosol forms a smaller proportion of atmospheric aerosol in the PD polluted atmosphere compared to PI conditions.

75   The definition of what atmospheric composition changes can be attributed to land use change can be expanded even further beyond the impacts on O_3, CH_4 and aerosols. Ward et al. (2014), in addition to impacts from BVOC and CO_2 emissions, considered changes in fire emissions and impacts from dust and smoke. This resulted in a SARF from land use change of $+0.9 \pm 0.5$ W m^{-2}, predominantly driven by CO_2. Heald and Geddes (2016) included emissions from agriculture, which can substantially contribute to nitrate aerosol, due to the use of nitrogen-based fertilisers. This increase in atmospheric aerosol
80   introduced a negative ARI forcing ($IRF_{ARI, nitrate} = -0.071$ W m^{-2}) that offset the positive forcing from the reduced biogenic SOA ($IRF_{ARI,SOA} = +0.017$ W m^{-2}). Overall, these studies highlight that the contributions from different trace gases and aerosols to the PI to PD land use change forcing remain uncertain and that the inclusion and representation of processes can have significant impacts on the calculated forcing.

The land use ERF calculated using versions 1.0 and 1.1 of UKESM was -0.17 ± 0.04 W m^{-2} and -0.21 ± 0.04 W m^{-2},
85   respectively (O'Connor et al., 2021; Mulcahy et al., 2023), which is similar to the early estimates by Unger (2014a,b). However, this forcing has not been decomposed into the various atmospheric chemistry and aerosol contributions in either version of UKESM. Further, new and improved parameterisations and process representations are now possible, which have been shown to impact radiative effect calculations (Sands et al., 2025). The relevant changes include: organically-mediated boundary layer nucleation (BLN), updated aerosol hygroscopicity, updated plant functional type (PFT) BVOC emission factors, the
90   contribution to SOA from isoprene as well as alternative representations (more complex) of gas phase chemistry in this model.

In this work, we evaluate the effective radiative forcing (ERF_{LU}) from PI to PD land use change, using UKESM with updated process representation. We further decompose the total land use forcing into the contributions from O_3, CH_4 and CO_2, as well as the aerosol direct and indirect effects, and surface albedo. This is the first attempt to decompose the PI to PD land use change forcing in UKESM in such detail; the ERF_{LU} will also be affected by processes missing in previous assessments. We introduce the model, experimental set up and the approaches used to calculate the radiative forcings of various components in section 2. In section 3, we present the newly-calculated land use ERF and the individual contributions, while section 4 includes the discussion and conclusions.

2 Methodology

2.1 Model description

This study employs an atmosphere-only configuration of the United Kingdom Earth System Model vn1.1 (UKESM1.1; Mulcahy et al. (2023)) at a resolution of N96L85, with the addition of several new or updated processes that are relevant to biogenic emission impacts on atmospheric chemistry and aerosols. The impact of these processes, which are detailed in the following paragraphs, has been previously assessed in a present-day climate simulation (Sands et al., 2025). The Global Atmosphere 7.1 science configuration of the Met Office's Unified Model (MetUM) (Walters et al., 2019) is used to simulate the physical atmosphere, while the United Kingdom Chemistry and Aerosols (UKCA) model (Morgenstern et al., 2009; O'Connor et al., 2014) with the Global Model of Aerosol Processes (GLOMAP-mode; Mann et al. (2010); Mulcahy et al. (2020)) are the chemistry and aerosol components.

The vegetation is represented by 13 plant functional types (PFTs), the distribution of which is prescribed based on a pre-existing coupled transient historical simulation of UKESM1.1. In this pre-existing simulation, the vegetation was interactive. Outputs from the same simulation are used to prescribe the canopy height and leaf area index (LAI) values. The PFT distribution and LAI drive BVOC emissions, for which the interactive biogenic volatile organic compound (iBVOC) scheme is used (Pacifico et al., 2011, 2012). A key difference in the model set up here compared to the standard UKESM1.1 is the use of updated isoprene and monoterpene emission factors (Weber et al., 2023).

Two mechanisms for fully interactive stratospheric and tropospheric chemistry are used in this study. StratTrop vn1.0 (ST; Archibald et al. (2020)) is the standard chemistry mechanism in UKESM1.1, while CRI-Strat 2 (CS2; Archer-Nicholls et al. (2021); Weber et al. (2021)) is a more complex scheme, which includes HO_x recycling during isoprene oxidation, the separation of lumped monoterpenes into α-pinene and β-pinene, and a more explicit oxidation scheme for both monoterpenes that includes the formation of trace gases, predominantly oxygenated VOCs. The schemes are referred to as the standard and complex mechanisms, respectively. In both mechanisms, monoterpenes and isoprene contribute to aerosol mass through the formation of condensable vapours (Sec_Org_{MT} and Sec_Org_I) which condense onto pre-existing particles. We further include organically-mediated boundary layer nucleation (BLN), through which Sec_Org_{MT} can contribute to new particle formation in the boundary layer.

GLOMAP-mode simulates four aerosol types: sulphate (SU), sea-salt (SS), black carbon (BC) and organic matter (OM). These are combined with the Coupled Large-scale Aerosol Simulator for Studies In Climate (CLASSIC) aerosol scheme for mineral dust (DU). We apply a correction to the hygroscopicity values of the different aerosol types, which includes an increase in the hygroscopicity of OM. Previous research has found that the response in ACI associated with increased OM are atypical in UKESM1.0 compared to other ESMs, which is attributed to relatively inefficient cloud nucleation (Thornhill et al., 2021b). This response may be affected by the change in hygroscopicity. Due to the coupling between the gas-phase chemistry and aerosols, the formation and growth of aerosol particles responds to changes in the simulated trace gases that are aerosol precursors, as well as changes in oxidants (e.g. O'Connor et al. (2021)).

2.2 Experimental set up

Calculation of the land use ERF is based on the comparison of a PI control (*piClim-control**) and an experiment where the only change is the use of land cover representative of the year 2014, assumed to be PD (*piClim-lu**) (Table 1). The difference between the experiment pairs (perturbation − control) represents the impact of changing land use. Each experiment was run for 45 model years. The results presented are based on the latter 30 years of model simulations, following the protocols from the Radiative Forcing Model Intercomparison Project (RFMIP) (Pincus et al., 2016) and recommendations from Forster et al. (2016).

We make use of a pre-existing experiment pair from UKESM1.1 (*piClim-control* and *piClim-lu*; Mulcahy et al. (2023)) and run two new key experiment pairs, which use two different chemistry mechanisms. Two simulations (*piClim-control_S* and *piClim-lu_S*) include the additional processes described in the previous subsection (section 2.1), except for the complex chemistry mechanism. As the complex chemistry mechanism has been found to have a substantial influence on BVOC impacts (Weber et al., 2022), it is included alongside other processes in the second experiment pair (*piClim-control_C* and *piClim-lu_C*). Two additional experiments (the pre-existing *piClim-CH4* and new *piClim-CH4_S*) were used to calculate the methane (CH$_4$) feedback factor on its own lifetime. Further, the *piClim-CH4_S* experiment can be used to calculate the CH$_4$ effective radiative forcing (ERF$_{CH4}$) associated with land use change.

2.3 Radiative forcing calculations

The net simulated land use effective radiative forcing (ERF$_{LU}$) is calculated based on the change in the net incoming (downwelling − upwelling) top of atmosphere (TOA) fluxes in both the shortwave (SW) and longwave (LW) between the land use perturbation experiment (*piClim-lu_S* or *piClim-lu_C*) and the respective control (*piClim-control_S* or *piClim-control_C*) simulations. The methodology to quantify the forcing associated with a particular gas, aerosol effects or surface albedo varies; the approaches used are described in more detail in the paragraphs below.

The recommendations of Ghan (2013) are followed to calculate the instantaneous radiative forcing (IRF) from aerosol-radiation interactions (IRF$_{ARI}$), as well as the cloud forcing from changes in cloud-radiative effects (ΔCRE):

$$IRF_{ARI} = \Delta(F - F_{clean}) \tag{1}$$

Table 1. Summary of the prescribed conditions of the fixed SST time-slice simulations. Three simulations are pre-existing (*piClim-control*, *piClim-lu* and *piClim-CH4*), while the other experiments were prepared specifically for this research. The standard chemistry mechanism is Strat-Trop vn1.0, while the complex chemistry refers to CRI-Strat 2. The methane column shows the prescribed values. *Other updates: inclusion of organically mediated boundary layer nucleation; updated hygroscopicity values, reaction rates and BVOC emission factors; contribution to SOA from isoprene.

Experiment name	Land use (PFT fractions, LAI, canopy height	Anthropogenic emissions	Methane ppb	Chemistry mechanism	Other updates*
piClim-control, Mulcahy et al. (2023)	1850	1850	808.25	Standard	No
piClim-lu, Mulcahy et al. (2023)	2014	1850	808.25	Standard	No
piClim-CH4, pre-existing	1850	1850	1831.47	Standard	No
piClim-control_S	1850	1850	808.25	Standard	Yes
piClim-lu_S	2014	1850	808.25	Standard	Yes
piClim-control_C	1850	1850	808.25	Complex	Yes
piClim-lu_C	2014	1850	808.25	Complex	Yes
piClim-CH4_S	1850	1850	768.76	Standard	Yes

155

$$\Delta CRE = \Delta(F_{clean} - F_{clear,clean}) \tag{2}$$

where F is the TOA radiative flux (downwelling − upwelling), F_{clean} is the TOA radiative flux excluding scattering and absorption by aerosols and $F_{clear,clean}$ is the TOA radiative flux excluding cloud effects and scattering and absorption by aerosols. The calculation of radiative fluxes multiple times with different forcings included is referred to as the double call method. The

160   aerosol-free fluxes are used to calculate the CRE, as aerosols above clouds also interact with the radiation and can bias the forcing diagnosis at TOA (Ghan, 2013).

A double call to the radiation scheme is also used to calculate the instantaneous radiative forcing driven by changes in ozone concentrations (IRF_{O3}). For each simulation, the radiative fluxes are calculated once using a reference O_3 distribution and once using the simulated O_3 concentrations. The same reference distribution data, in this case monthly mass mixing ratios for the

165   year 2014, are used for all simulations, so that the difference between the reference and simulated O_3 radiative fluxes can be compared between simulations to calculate IRF_{O3} (Collins et al., 2025).

The surface albedo forcing ($RF_{Alb, surf}$) is calculated following Weber et al. (2024):

$$RF_{Alb} = \Delta F_{surf,clear,clean} \times \frac{SW_{DW,surf,clean}}{SW_{DW,surf,clear,clean}} \tag{3}$$

where $F_{surf,clear,clean}$ is the surface flux excluding scattering by aerosols and clouds, and ($SW_{DW,surf,clean}$ / $SW_{DW,surf,clear,clean}$) is the

170   ratio of the downwelling SW clean (excluding scattering and absorption by aerosols) to SW clear-clean (excluding scattering

and absorption by aerosols and clouds) fluxes at the surface. This method is used so that the albedo effect is not amplified by the removal of the cloud and aerosol effects, which permits a higher proportion of SW radiation to directly reach the surface/TOA. However, the $RF_{Alb, surf}$ is quantified at the surface, whereas the aerosol and O_3 forcings are calculated at the TOA. The presence of SW absorbing trace gases and aerosols in the atmosphere means not all of the reflected radiation would reach the TOA.

175   Two alternative surface albedo forcing calculations, which are valid at the TOA, are also explored to test the sensitivity of this result to the methodology. The simplest method makes the assumption that the change in SW TOA fluxes excluding scattering and absorption by aerosols and clouds is predominantly due to changes in surface albedo (Ghan, 2013), so that

$$RF_{Alb,clear,clean,TOA} = \Delta F_{SW,clear,clean}. \tag{4}$$

This method is expected to overestimate the albedo forcing, as the masking effect of clouds and aerosols is completely removed.
180   Finally, the forcing can be estimated from the clear-sky change in surface albedo, the incident SW radiation at the top of atmosphere and the clear-sky atmospheric transmissivity (0.7) following Qu and Hall (2006) and Collins et al. (2025):

$$RF_{Alb,clear,TOA} = -0.7 \times \Delta Albedo \times SW_{DW,TOA}. \tag{5}$$

This method includes a correction for the effects of gases and aerosols in the atmosphere that interact with the reflected SW radiation and provides an estimate for the TOA surface albedo forcing. However, the masking effect of clouds is not included.
185   The impacts of changes to CH_4 and CO_2 are not included in the net ERF_{LU} calculated from the land use perturbation simulation pairs, as the concentrations of both greenhouse gases are prescribed. Two methods are used to calculate the CH_4 forcing for the standard chemistry mechanism, but only method one is applied for the complex chemistry mechanism due to the high computational cost of the second approach. The first method follows a multi-step process to estimate the RF_{CH4} based on the change in CH_4 concentration expected from the difference in CH_4 lifetime between the simulation pairs. The
190   CH_4 lifetime for each simulation is initially calculated against removal by OH, but adjusted for stratospheric and soil sinks, following Holmes (2018). Next, the change in CH_4 concentration based on these lifetimes is calculated as in multiple previous studies (e.g. O'Connor et al., 2021; Weber et al., 2024; Stevenson et al., 2013; Fiore et al., 2009):

$$[CH4]_{piClim-LU} = [CH4]_{piClim-control} \times (\frac{\tau_{piClim-LU}}{\tau_{piClim-control}})^f \tag{6}$$

where [CH4] is the CH_4 concentration, τ is the CH_4 lifetime and f is the feedback factor accounting for the feedback of CH_4 on
195   its own lifetime (Prather, 1996). Changes in CH_4 affect OH concentrations, which in turn impact CH_4 oxidation and lifetime (O'Connor et al., 2010; Voulgarakis et al., 2013). We note the CH_4 feedback on its own lifetime varies depending on the Earth system model and background state of the atmosphere. We first calculate f based on outputs from pre-existing UKESM1.1 simulations (piClim-control and piClim-CH4) and the following equations:

$$f = 1/(1 - s) \tag{7}$$

200   where:

$$s = \frac{\Delta ln\tau}{\Delta ln[CH4]}. \tag{8}$$

Next, the direct radiative effect from changes in CH_4 concentrations is calculated following Etminan et al. (2016):

$$RF_{CH4init} = [a\bar{M} + b\bar{N} + 0.043] \times (\sqrt{M} - \sqrt{M_0}) \tag{9}$$

where a and b are constants (a $= -1.3 \times 10^{-6}$ W m^{-2} ppb^{-1} and b $= -8.2 \times 10^{-6}$ W m^{-2} ppb^{-1}), M is the concentration of CH_4
(ppb) that would arise following the land cover change if the modelled concentration was free to evolve, M_0 is the prescribed
PI concentration, while $\bar{M}$ is the mean of the two concentrations of CH_4. $\bar{N}$ refers to the PI concentration of N_2O (ppb) in this
case. Finally, $RF_{CH4init}$ is scaled to account for methane's indirect radiative effects due to its impacts on O_3 and stratospheric
water vapour production, as well as the cloud radiative effect. Previous research based on multi-model assessments suggested a
scaling of 1.31 (Smith et al., 2018; Thornhill et al., 2021a; Weber et al., 2024). However, this scaling may not be representative
of UKESM. Instead, the decomposition of the CH_4 forcing specifically in UKESM1.0 (O'Connor et al., 2022) is used to
estimate the scaling. This UKESM-specific scaling is between 1.43 and 1.96 based on the ratio of the total PI-to-PD ERF$_{CH4}$,
which includes all indirect effects, to the PI-to-PD ERF from changes in CH_4 concentrations alone. The range represents the
uncertainty in the simulation results. The indirect radiative effects of CH_4 are assumed to scale linearly with the magnitude of
the change in CH_4 concentration for this calculation.

The second method to calculate the CH_4 forcing is based on the additional experiment piClim-CH4_S introduced in the
previous section, for which the CH_4 concentration calculated in method one was prescribed. The difference in TOA fluxes
between piClim-CH4_S and piClim-control_S represents the ERF$_{CH4}$ when the standard chemistry mechanism is used. We
also use the comparison between these two simulations to calculate the CH_4 feedback on its own lifetime in our modelling set
up; we find that the difference between UKESM1.1 and the model set up used here with the standard chemistry mechanism is
not substantial (1.31 vs 1.29). We were not, however, able to calculate a separate estimate for the feedback when the complex
chemistry is used with the available simulations.

Finally, the CO_2 forcing (RF_{CO2}) from the land use change is calculated following Etminan et al. (2016):

$$RF_{CO2} = [a_1(C - C_0)^2 + b_1|C - C_0| + c_1\bar{N} + 5.36] \times ln(C/C_0) \tag{10}$$

where a_1, b_1 and c_1 are constants ($a_1 = -2.4 \times 10^{-7}$ W m^{-2} ppm^{-1}; $b_1 = 7.2 \times 10^{-4}$ W m^{-2} ppm^{-1}, $c_1 = -2.1 \times 10^{-4}$ W m^{-2}
ppb^{-1}), C is the concentration of CO_2 (ppm) that would arise following the land cover change if the modelled concentration was
free to evolve, C_0 is the prescribed PI concentration, while $\bar{N}$ refers to the PI concentration of N_2O (ppb). The change in CO_2
concentration is calculated based on the historical land use carbon emission data provided for the Coupled Climate–Carbon
Cycle Model Intercomparison Project (C4MIP) (Jones et al., 2016). An airborne fraction of 0.5 for the carbon emissions
(Bennett et al., 2024) is used to calculate the resulting change in atmospheric CO_2.

3 Results

3.1 Land cover change between 1850 and 2014

The PI to present-day PD land use change is dominated by the loss of forest cover, both broadleaf and needleleaf, in favour of grasslands (Figure 1). Regions of particularly substantial change include central and eastern North America and the southern hemisphere (SH) (sub)tropics, where some areas lose over 50% of their forest cover. The northern hemisphere (NH) mid-to-high-latitude changes involve both broadleaf and needleleaf forests, while predominantly broadleaf forests are diminished at low latitudes (Figure 1e). Smaller scale changes occur in southern Africa and central Eurasia. Conversely, in the European Alps, grasses are replaced by shrubs and needleleaf forests. Overall, the PI to PD land use change results in a loss of 14% of the global forest cover (Table 2), which drives a decrease in the global mean leaf area index (LAI) by 0.16 (-8%).
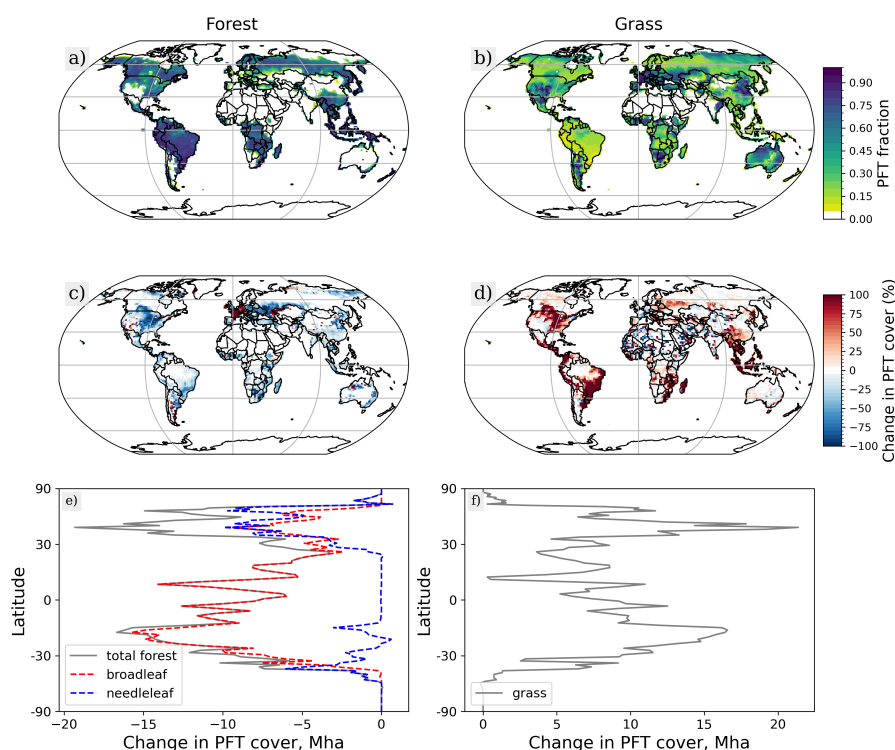
Figure 1. Distribution of the forest (left column) and grass (right column) PFTs. Panels a) and b) show the spatial distribution used to represent land cover for 1850. Panels c) and d) show the change from pre-industrial to present-day conditions (2014 − 1850) as a % of the 1850 PFT distribution. Panels e) and f) show the total change in forest (broadleaf and needleleaf) and grass as a function of latitude.

Table 2. Baseline (*piClim-control_S* or *piClim-control_C*) values of key variables for both the standard and complex chemistry mechanisms, as well as their relative differences in response to pre-industrial to present-day land use change (e.g. *piClim-LU_S − piClim-control_S*). The baseline values are given as global sums, except for the BVOC lifetimes, total column ozone (TCO$_3$), methane concentration, cloud droplet number concentration (CDNC), and surface OH concentration, for which the surface area weighted global mean values are presented.

Variable	Standard chemistry		Complex chemistry	
	piClim-control_S	*piClim-LU_S* − *piClim-control_S*	*piClim-control_C*	*piClim-LU_C* − *piClim-control_C*
Tree cover	5740 Mha	−14%	5740 Mha	−14%
Grassland	4356 Mha	+17%	4356 Mha	+17%
LAI	2.03	−8%	2.03	−8%
Isoprene emissions	635 Tg(C$_5$H$_8$) yr^{-1}	−18%	636 Tg(C$_5$H$_8$) yr^{-1}	−18%
Isoprene burden	1.14 Tg(C$_5$H$_8$)	−25%	0.48 Tg(C$_5$H$_8$)	−24%
Isoprene lifetime	15.56 hr	−8%	6.58 hr	−7%
Monoterpene emissions	122 Tg(C$_{10}$H$_{16}$) yr^{-1}	−16%	123 Tg(C$_{10}$H$_{16}$) yr^{-1}	−16%
Monoterpene burden	0.08 Tg(C$_{10}$H$_{16}$)	−20%	0.07 Tg(C$_{10}$H$_{16}$)	−21%
Monoterpene lifetime	5.97 hr	−5%	4.72 hr	−5%
TCO$_3$	333 DU	+0.05%	335 DU	−0.2%
Methane	777 ppbV	−5%	776 ppbV	−3%
Sec_Org$_I$	96,079 kg	−27%	72,257 kg	−24%
Sec_Org$_{MT}$	37,491 kg	−19%	44.284 kg	−19%
OM	1.38 Tg	−4%	1.31 Tg	−3%
SU	0.26 Tg	+2%	0.19 Tg	+1%
CDNC at 1000 m	28 cm^{-3}	−0.3%	26 cm^{-3}	−0.3%
Surface OH	1.15×10^6 molec. cm^{-3}	+4%	1.25×10^6 molec. cm^{-3}	+3%

3.2 Impact of land cover change on BVOC emissions

240 Consistent with the decrease in high-BVOC-emitting forests in favour of grasslands, the global emissions of isoprene and monoterpenes decrease by around 115 Tg(C$_5$H$_8$) yr^{-1} (−18%) and 20 Tg(C$_{10}$H$_{16}$) yr^{-1} (−16%), respectively, as a result of the land cover change (Table 2, Figure 2), which is comparable to the decrease in BVOC emissions estimated in previous studies of PI to PD land cover impacts (Heald and Spracklen, 2015). The spatial pattern of decreased emissions closely follows that of forest cover loss (or, conversely, grass cover gain). However, the magnitude of the decrease in BVOC emissions is greatest

245 in the tropics. This is due to the higher emission factors of broadleaf forest PFTs, which form a greater proportion of the deforestation at low latitudes, as opposed to needleleaf forest PFTs (compare Fig. 1e and Fig. 2e). The decreased emissions lead to decreases in the global burden of isoprene and monoterpenes by 20% to 25% (Table 2).

The global burdens of both isoprene and monoterpenes are much lower for the simulations with more complex chemistry (Table 2), despite very similar BVOC emission magnitudes. This is driven by the higher oxidising capacity of the atmosphere

250 when the complex mechanism is used (Archer-Nicholls et al., 2021; Weber et al., 2021), driving a 58% (21%) decrease in
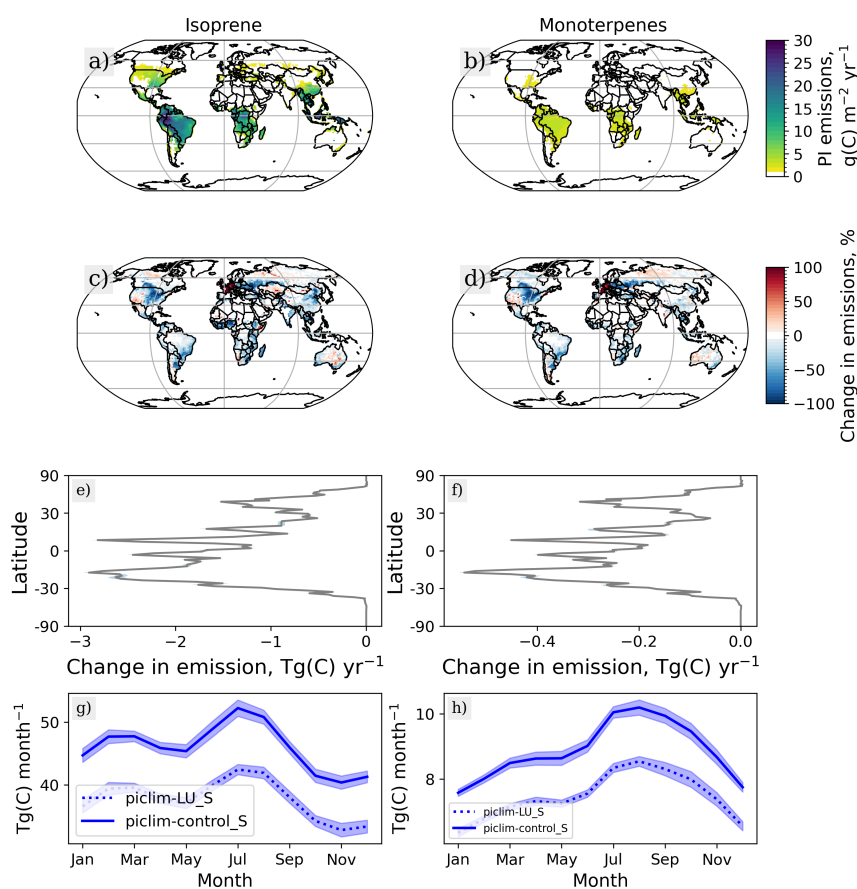
Figure 2. Land cover change impact on BVOC emissions (left column: isoprene, right column: monoterpenes). Panels a) and b) show the mean annual emissions of isoprene and monoterpenes for pre-industrial conditions. Panels c) and d) show the relative change in the respective emissions when present-day land cover is used. The absolute latitudinal differences are shown on panels e) and f), while the the global seasonal cycles from the *piClim-control_S* and *piClim-LU_S* experiments are displayed on panels g) and h).

isoprene (monoterpene) lifetime compared to the standard mechanism in the PI simulations. However, the relative change in BVOC burden and lifetime due to land use is largely consistent. For both chemistry mechanisms, the land use-driven decreases in burden are driven by the lower BVOC emissions combined with the 5% to 8% shorter lifetimes in the land use perturbation experiments. We attribute these shorter lifetimes to the greater availability of oxidants near source regions when

255   BVOC emissions are decreased following land use changes; the surface level OH concentrations increase by 3% to 4% (Table 2).

3.3   Net simulated PI to PD ERF_{LU}

Figure 3 shows the net simulated effective radiative forcing from PI to PD land use change (ERF_{LU}) for the standard and complex chemistry experiment pairs. The global mean ERF_{LU}, which excludes the CO_2 and CH_4 contributions, is -0.080 ± 0.047

260   W m^{-2} with the standard chemistry scheme, while the magnitude of the forcing increases for the complex chemistry scheme to -0.116 ± 0.041 W m^{-2}. The regional nature of land use change results in significant and substantial regional differences in TOA fluxes, despite the relatively small global mean ERF_{LU}. The dominant latitudinal feature is, on average, the -0.5 W m^{-2} or -1.0 W m^{-2} forcing at around 50°N for the standard and complex chemistry mechanisms, respectively (Figure 3b,d), which is consistent with the substantial loss of forest cover at these latitudes. For both mechanisms, the negative forcing is particularly

265   substantial over eastern Europe and central North America, where it regionally reaches -8 W m^{-2}. The greater magnitude of the NH forcing when employing more complex chemistry is driven by changes in northeast Asia (Fig. 3c); a negative forcing in this region is not present with the standard chemistry scheme.

The other substantial difference between the simulations with different chemical mechanisms occurs in the southern high latitudes, where the latitudinal mean ERF_{LU} rises to +0.4 W m^{-2} when using the standard scheme but is strongly negative

270   (below -0.5 W m^{-2}) for the complex chemistry scheme. This latitudinal signal is driven predominantly by regional differences in East Antarctica, which we connect to changes in O_3 (discussed in more detail in section 3.6). The results tend to be more consistent at the lower latitudes, especially in the SH, where the ERF_{LU} values lie between -0.25 and 0.25 W m^{-2}, despite the substantial deforestation in the (sub)tropical SH.
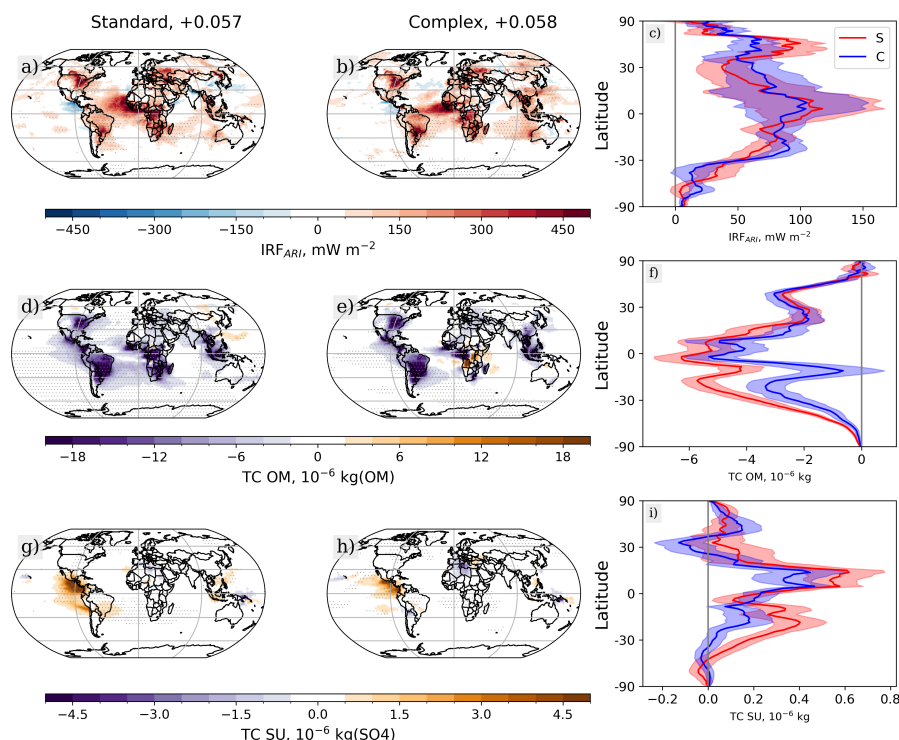
3.4   Aerosol-radiation interactions

275   Figure 4 a-c shows the mean instantaneous radiative forcing associated with the aerosol direct effect (IRF_{ARI}) from land use change. The global average IRF_{ARI} is $+0.057 \pm 0.015$ W m^{-2} and $+0.058 \pm 0.011$ W m^{-2} for the standard and complex chemistry mechanisms, respectively. In both cases, the shortwave forcing dominates (+0.058 W m^{-2} and +0.056 W m^{-2} for the standard and complex mechanisms, respectively; Table 3). IRF_{ARI} values tend to increase closer to the equator, although there is a secondary peak in the forcing in the NH mid-to-high-latitudes (Fig. 4c).

280   The positive IRF_{ARI} values are driven by a decrease in aerosol burden, which results in less scattering and reflection of SW radiation. Global organic matter (OM) burdens decrease by 3% to 4% (Table 2). Figure 4 d-f shows how the decreases in total column OM occur in the same regions as the positive IRF_{ARI}. The decreases are also greatest near the equator, where the BVOC emissions decrease by the greatest amounts (section 3.2), and where the highest magnitude of IRF_{ARI} is found. The magnitude
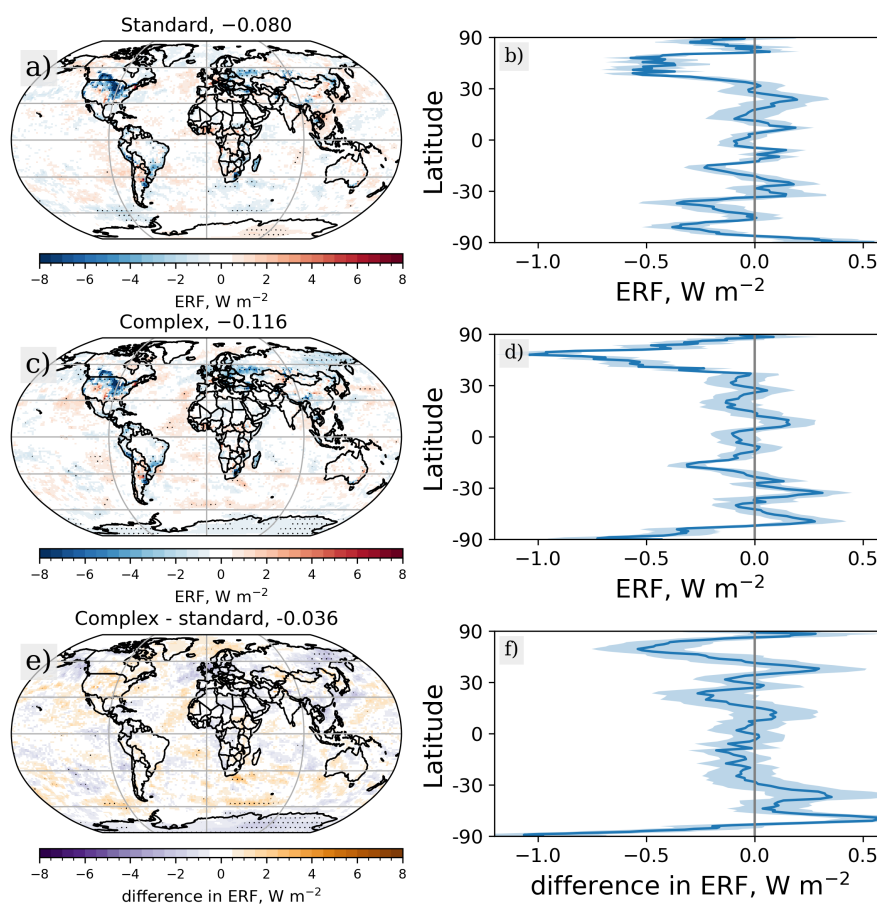
Figure 3. Net simulated TOA land use ERF (ERF_{LU}) in W m^{-2} for the standard chemistry mechanism (a), as well as respective zonal mean values (b). Panels c) and d) are the equivalent data for the complex chemistry mechanism. Values over panels a) and c) are the global mean ERFs. Panel e) shows the geographical distribution of the difference in ERF_{LU} when the chemistry mechanism is changed and panel f) shows the zonal change in ERF_{LU}. Stippling on subplots a), c) and e) shows differences that are significant based on Student's t-test with 95% confidence, while shading on the zonal plots shows the standard error.

Figure 4. The role of aerosol-radiation interactions in pre-industrial to present-day land use forcing. Subplots a-c show the top of atmosphere IRF from ARI associated with land cover changes for the standard (s, left column) and complex (c, middle column) chemistry mechanism, as well as the zonal mean values of IRF$_{ARI}$ values for both mechanisms (right column). The changes in total column organic matter (OM) mass are displayed in subplots d), e) and f), while subplots g), h) and i) show the differences in total column sulphate (SU) mass. Stippling in the left and middle columns shows regions of significant differences based on Student's t-test with 95% confidence, while shading on the zonal plots shows the standard error.

of the decrease in OM mass is slightly greater for the standard chemistry mechanism than for the more complex mechanism, particularly in the SH. As the atmospheric oxidation capacity is lower when the standard mechanism is used, trace gases have longer lifetimes and can be transported further from source, resulting in the changes secondary aerosol occurring over a greater area (compare Fig. 4 d and e).

While the global mean IRF$_{ARI}$ values are positive, we note there are some regions of significant negative forcing, particularly in Central America. These regional impacts can be connected to an increase in sulphate aerosol in these regions (Fig. 4 g-i). The decrease in BVOC emissions and burden under land use change increases the availability of the hydroxyl radical (OH), one of the main oxidants of sulphur dioxide (SO$_2$). As a result, aerosol formation and growth reactions occur closer to source regions, leading to greater sulphate aerosol burdens in these areas. Additionally, a slight shift occurs in the sulphate formation and growth pathways; there is an <2 percentage point increase in the relative contribution from reactions with OH, potentially

Table 3. Decomposition of the pre-industrial to present-day land use radiative forcing in mW m^{-2}.

Forcing	Standard chemistry			Complex chemistry		
	LW	SW	net	LW	SW	net
ERF_{LU}	$+19 \pm 28$	-99 ± 37	-80 ± 46	$+36 \pm 32$	-152 ± 27	-116 ± 42
IRF_{ARI}	-1 ± 5	$+58 \pm 19$	$+57 \pm 15$	$+2 \pm 4$	$+56 \pm 15$	$+58 \pm 11$
ΔCRE	$+1 \pm 14$	$+86 \pm 30$	$+87 \pm 33$	$+35 \pm 19$	$+47 \pm 27$	$+82 \pm 25$
IRF_{O3}	-7 ± 5	$+4 \pm 8$	-3 ± 12	-10 ± 4	-5 ± 6	-15 ± 9
$RF_{Alb, surf}$		-174 ± 6			-169 ± 12	
ERF_{CH4} simulated	$+39 \pm 32$	-54 ± 28	-15 ± 32			
ERF_{CH4} calculated			-46 ± 8			-27 ± 5
RF_{CO2}			$+867 \pm 87$			$+867 \pm 87$

leading to a shift to more numerous but smaller sulphate particles (Karset et al., 2018; O'Connor et al., 2022). The impacts on

295 sulphate aerosol are greater for the standard mechanism, where the oxidation capacity is more sensitive to changes in BVOC emissions (Sands et al., 2025).

3.5 Cloud radiative effect

Figure 5 a-c shows the change in the temporal average cloud radiative effect (ΔCRE) associated with pre-industrial (PI) to present-day (PD) land use change. The magnitude of the global mean ΔCRE is very similar for both the standard chemistry

300 mechanism ($+0.087 \pm 0.033$ W m^{-2}) and the complex mechanism ($+0.082 \pm 0.025$ W m^{-2}). However, the effect is almost limited to changes in the SW for the standard mechanism ($\Delta CRE_{SW} = +0.086 \pm 0.030$ W m^{-2}), whereas LW fluxes are more affected for the complex mechanism ($\Delta CRE_{SW} = +0.047 \pm 0.027$ W m^{-2}, $\Delta CRE_{LW} = +0.035 \pm 0.019$ W m^{-2}; Table 3), although the decomposed ΔCRE still overlap due to the substantial standard error.

The ΔCRE tends to be positive over regions of substantial deforestation, such as central North America and eastern South

305 America. The positive ΔCRE_{SW} is likely due to the changes in aerosols, introduced in the previous section (section 3.4), driving a decrease in the cloud droplet number concentration (CDNC) as the aerosol burden is reduced. The CDNC at 1 km altitude tends to decrease over regions of deforestation (Fig. 5 d-f), in turn leading to an increase in the effective radius of the cloud droplets (Fig. 5 g-i). These changes decrease the amount of incoming radiation reflected by the cloud, resulting in a positive forcing (i.e. the so-called Twomey effect is weaker (Twomey, 1977)).

310 The method for calculating the ΔCRE used in this study will also capture differences due to changes in cloud amount and/or the location and lifetime of clouds, all of which may also be influenced by changes in water vapour or atmospheric dynamics. While the impacts of these changes are not investigated separately in detail here, and they may contribute to noted difference in ΔCRE_{SW}, the spatial pattern of ΔCRE_{LW} closely resembles the changes in average cloud amount at 10 km altitude (Fig. 6). This high-altitude cloud amount increases over a 3% larger area when the complex chemistry mechanism is used. The greater

315 change in ΔCRE_{LW} with the complex mechanism could be driven by these differences in high-level clouds. An increase in cirrus-type clouds reduces the amount of outgoing LW radiation and leads to a positive forcing (Chen et al., 2000).
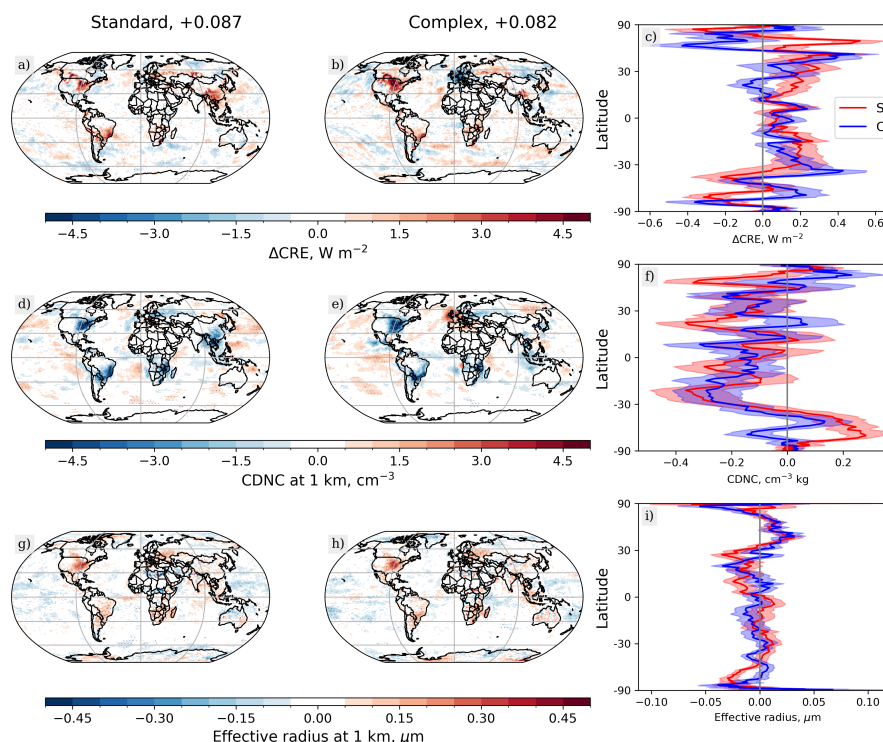
Figure 5. The role of the cloud radiative effect (CRE) in pre-industrial to present-day land use forcing. Subplots a-c show changes in the top of atmosphere fluxes from ΔCRE associated with land cover changes for the standard (s, left column) and complex (c, middle column) chemistry mechanism, as well as the zonal mean ΔCRE values for both mechanisms (right column). The changes in cloud droplet number concentrations (CDNC) at 1km altitude are displayed in subplots d), e) and f), while subplots g), h) and i) show the differences in effective radius at 1km altitude. Stippling in the left and middle columns shows regions of significant differences based on Student's t-test with 95% confidence, while shading on the zonal plots shows the standard error.

3.6 O_3 contribution to ERF_{LU}

The mean O_3 instantaneous radiative forcing (IRF_{O3}) associated with the pre-industrial (PI) to present-day (PD) land use change is shown in Figure 7 a and b. While the global mean values are weakly negative (-0.003 ± 0.012 W m^{-2} and $-0.015 \pm$ 0.009 W m^{-2} for the standard and complex chemistry mechanisms, respectively), the standard errors are substantial and there are regions of positive forcing, particularly in regions associated with the NH polar jet stream. The major difference between the two chemistry mechanisms is the sign of IRF_{O3} over East Antarctica, which seems to be driving the difference in ERF_{LU} between the two mechanisms in this region. For the standard chemistry mechanism, the IRF_{O3} is positive ($<+0.1$ W m^{-2}) here, whereas the complex chemistry results in a negative forcing of a similar magnitude.

The changes in total column O_3 are mostly insignificant, though some significant differences closely resemble the patterns in IRF_{O3} at latitudes over 30° (Fig. 7c,d). Looking at the O_3 vertical distribution allows for more insight into changes in O_3

16
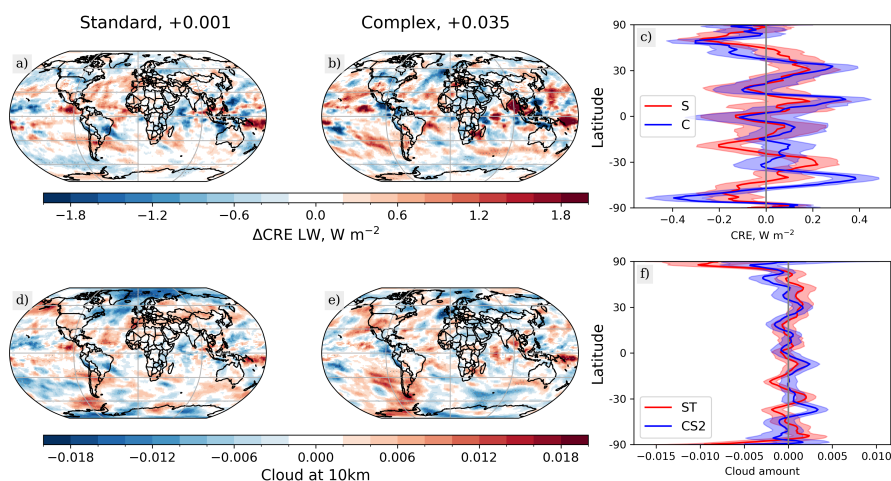
Figure 6. The change in longwave cloud radiative effect between present-day and pre-industrial conditions for the standard (a) and complex (b) chemistry mechanism, as well as the zonal mean values for both (right column). The change in cloud amount (as a fraction of the grid cell) at 10 km altitude for the standard (d) and complex (e) chemistry mechanisms, and the zonal mean cloud amount for both (f).

and subsequent IRF_{O3} impacts. While the O_3 volume mixing ratio tends to decrease in the troposphere, some increases in O_3 mixing ratios occur at the tropopause and in parts of the stratosphere (Fig. 7e,f). The tropospheric O_3 decrease may be driven by the loss of BVOCs, which are O_3 precursors. However, monoterpenes only act as an O_3 precursor in the complex chemistry mechanism, but not in standard scheme (Weber et al., 2021), thus the negative IRF_{O3} is of a greater magnitude for the complex scheme. We suggest the higher altitude changes in O_3 mixing ratios are driven by dynamical processes. To assess the dynamical influence, the changes in the age of air are shown in Fig. 7g,h. These highlight that the same locations around the tropopause that are associated with substantial differences in O_3 mixing ratios are affected by changes in transport timescales between the troposphere and stratosphere.

3.7 Impact of change to CH₄ lifetime

The experimental set-up includes prescribed methane (CH_4) concentrations, therefore limiting the impact land use change can have on the contribution to ERF_{LU} from CH_4 forcing. However, as changes in the abundance of BVOCs can affect CH_4 lifetime through changing the availability of OH, we can estimate the change in CH_4 concentration due to land use change (Holmes, 2018). We find the CH_4 lifetime against loss by OH decreases by 4% and 3% for the standard and complex mechanisms (Table 4) as a result of land use change, leading to lower equilibrium CH_4 concentrations by 37 ppbv and 23 ppbv, respectively. The impact is greater for the standard chemistry scheme, which is consistent with the greater sensitivity of atmospheric oxidants to BVOC emissions for this mechanism.

Following the calculated decrease in CH_4 concentrations from PI to PD land use change, the CH_4 effective radiative forcing (ERF_{CH4}) is negative. The comparison of the additional simulation *piClim-CH4_S* (see sections 2.2 and 2.3), which is set

17
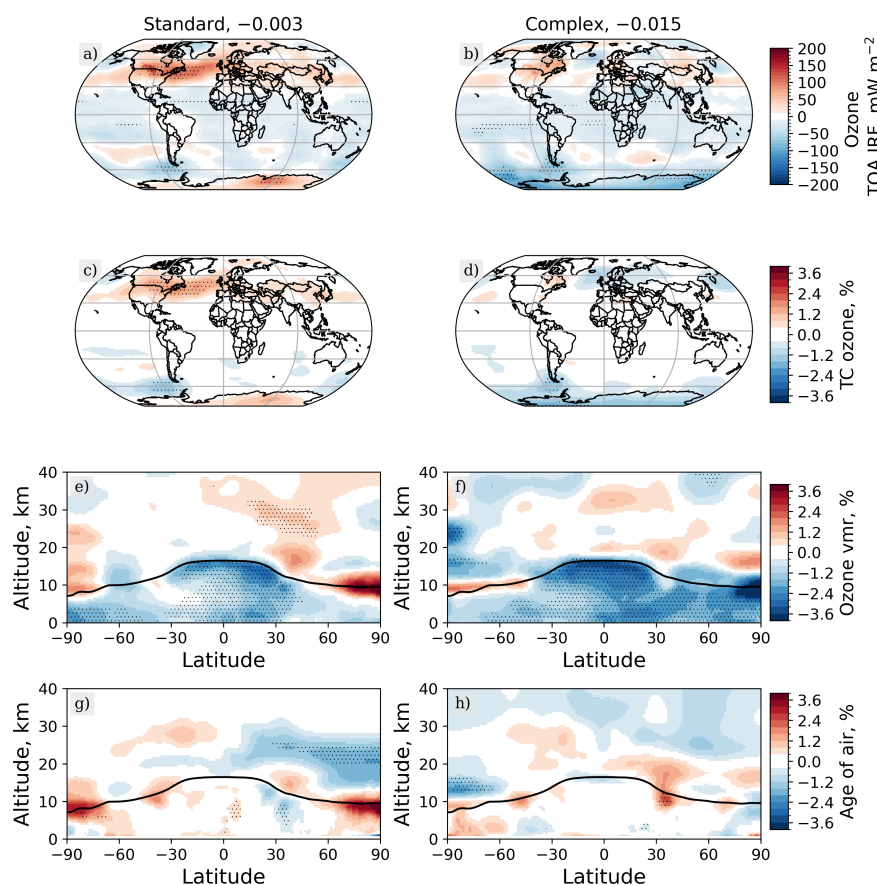
Figure 7. Contribution to pre-industrial to present-day land use forcing from changes in ozone. Changes in the TOA IRF from changes in O_3 concentrations in mW m^{-2} for the standard (a, left column) and complex (b, right column) chemistry mechanisms are compared to changes in TC O_3 (c, d). Values above subplots a) and b) show the global mean IRF$_{O3}$ in W m^{-2}. Changes in tropospheric and stratospheric O_3 volume mixing ratios are shown on subplots e) and f), while the change in the age of air is displayed on subplots g) and h). Stippling indicates significant differences based on Student's t-test with 95% confidence, while the black line on subplots e-h shows the mean height of the tropopause calculated within the model.

Table 4. CH_4 lifetimes against OH in the simulations alongside the global mean CH_4 concentrations and top of atmosphere effective radiative forcings from the calculated change in concentration or comparison against *piClim-control_S* for the CH_4 simulation. Note the CH_4 mixing ratios are calculated from model outputs and vary slightly from the prescribed values.

	Standard chemistry		Complex chemistry		CH_4 simulation
	Base	Exp	Base	Exp	
CH_4 lifetime against OH (yr)	8.70	8.33	7.60	7.41	8.59
CH_4 concentration (ppb)	777	740	776	753	740
CH_4 TOA ERF (mW m^{-2})	-46 ± 8		-27 ± 5		-15 ± 32

345   up with a prescribed global mean CH_4 concentration of 740 ppbv consistent with the calculated CH_4 decrease of 37 ppbv, and *piClim-control_S* suggests the global mean ERF_{CH4} is -0.015 ± 0.043 W m^{-2} (Table 3). This forcing estimate overlaps with the ERF_{CH4} values calculated using the Etminan et al. (2016) equations and additional scalings (see section 2.3) when considering the substantial uncertainty. Based on these calculations, the impact is of a greater magnitude for the standard chemistry (-0.046 ± 0.008 W m^{-2}) than the complex chemistry (-0.027 ± 0.005 W m^{-2}; Table 4), following the different
350   magnitudes of the changes in concentrations.

3.8   Impacts of biogeophysical effects and changes in CO_2 concentrations

While the focus of this research is on the non-CO_2 biogeochemical impacts of land use change, we recognise that CO_2 emissions, surface albedo and other biogeophysical effects, such evapotranspiration and surface roughness, will also have radiative effects. Here, we quantify the impacts of CO_2 and surface albedo for comparison with non-CO_2 atmospheric composition
355   forcings.

The changes in surface albedo are factored into the net simulated ERF_{LU}, alongside other geophysical impacts of land cover change, such as differences in evapotranspiration driving changes in water vapour. The global mean surface albedo forcing ($RF_{Alb, surf}$; Fig. 8a) calculated following Weber et al. (2024) is similar when using the standard and complex chemistry mechanisms at -0.174 ± 0.016 W m^{-2} and -0.169 ± 0.012 W m^{-2}, respectively (Table 3). Both of these estimates are within the
360   Intergovernmental Panel on Climate Change (IPCC) land use albedo ERF estimate of -0.2 ± 0.1 W m^{-2} (IPCC, 2023). Note that $RF_{Alb, surf}$ is not calculated at the TOA and therefore may not be directly comparable to other forcings that are calculated at the TOA. The alternative TOA calculations of the albedo forcing (-0.247 ± 0.017 W m^{-2} and -0.243 ± 0.019 W m^{-2}) remain within the IPCC land use albedo ERF estimate. The global mean surface albedo forcing values are, however, greater for both of the alternative methods as they do not account for the masking effect of clouds, which likely leads to an overestimation of
365   the forcing (Fig. 8).
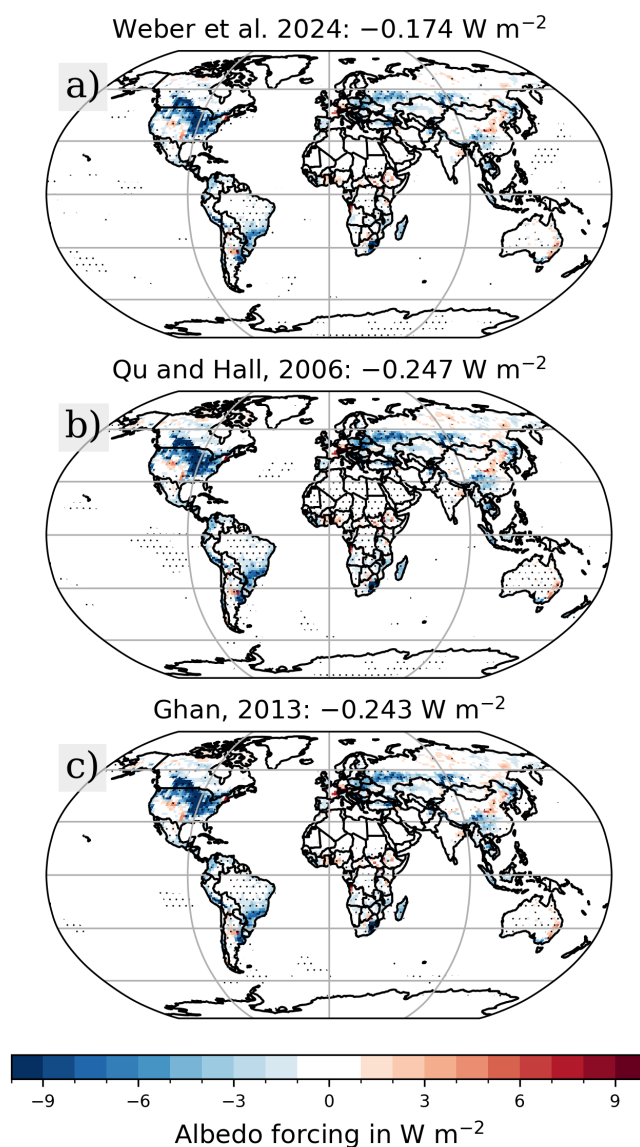
Figure 8. Comparison of 3 methods for albedo forcing calculation based on the experiments employing the standard chemistry mechanism. Panel a) shows the surface albedo forcing following Weber et al. (2024), which is valid at the Earth's surface, panel b) shows the change in clear-sky surface fluxes scaled by the clear-sky atmospheric transmissivity (estimated to be 0.7) to get a planetary albedo impact at the TOA (Qu and Hall, 2006; Collins et al., 2025), while panel c) shows the change in the clear and clean TOA fluxes, thought to be largely due to changes in surface albedo (Ghan, 2013). The stippling shows areas of significant change.

The CO_2 forcing, similarly to that of CH_4, is not included in ERF_{LU}, due to the prescribed CO_2 concentrations in the experimental set-up. Based on an airborne fraction of 0.5 and the C4MIP land use change carbon emissions (section 2.3), we calculate that atmospheric CO_2 would have increased by 392 $TgCO_2$ following the emission of around 214 TgC from land use change between 1850 and 2014. This is equivalent to an increase in atmospheric CO_2 by around 50 ppm. Using the equation from Etminan et al. (2016), this change in CO_2 results in a radiative forcing (RF_{CO2}) of $+0.867 \pm 0.087$ W m^{-2}.

3.9 Overview of decomposed LU forcing

In this section, we consider the relative impacts from each of the contributions to the land use change forcing. The largest magnitude forcings associated with changes in atmospheric composition, not including CO_2, are driven by IRF_{ARI} and ΔCRE (Figure 9). These, particularly in combination, are much greater than IRF_{O3} or ERF_{CH4}. However, the global mean ERF_{LU}, despite not including the negative ERF_{CH4}, is negative, which is connected to the biogeophysical effects. $RF_{Alb, surf}$ is of a much greater magnitude than the non-CO_2 biogeochemical forcings. Therefore, $RF_{Alb, surf}$ drives the negative sign of ERF_{LU}, while the changes in atmospheric trace gases and aerosols modify the magnitude of the net forcing.
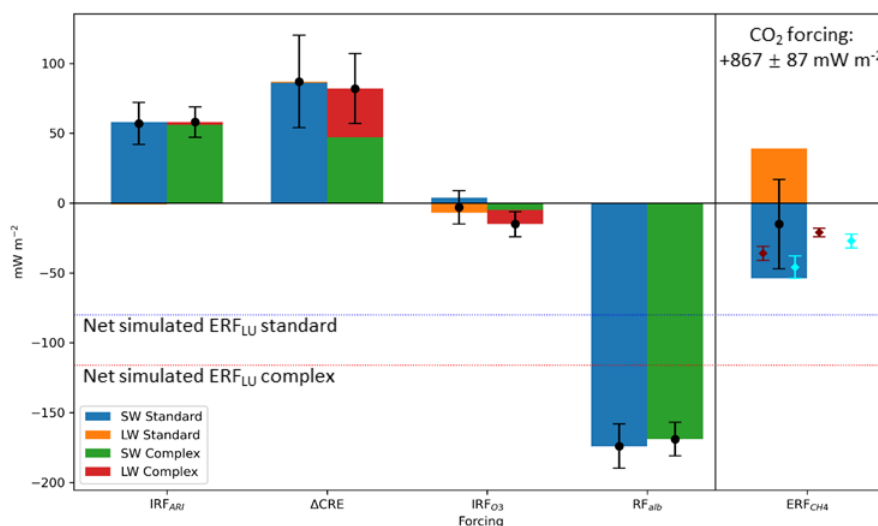
Figure 9. Comparison of forcings for the standard and complex chemistry mechanisms. Note the CH_4 and CO_2 forcing are not included in the net simulated TOA land use ERF, as both of these greenhouse gases are prescribed in the main simulation pairs. The cyan diamonds show the methane forcing calculated using scaling specific to the UKESM, while the maroon diamonds are based on the multi-model scaling.

The non-CO_2 forcings in combination, that is $ERF_{LU} + ERF_{CH4}$, offset only around 15% of the positive CO_2 forcing from PI to PD land use change emissions. Assuming ERF_{LU}, ERF_{CH4} and RF_{CO2} combine linearly, the total PI to PD land use change forcing based on our results is around +0.74 W m^{-2}, or 34% [25% to 48%] of the change in the net anthropogenic ERF from 1850-1900 to 2006-2019 (IPCC, 2019).

Table 5. Summary of the land use radiative forcing based on top-of-atmosphere fluxes for the standard versions of UKESM1.0 and UKESM1.1, as well as the new simulations presented in this research. NET'$_{CS}$ is clear-sky forcing that combines changes in trace gases, for example O_3, and in IRF$_{ARI}$.

Experiment pair	Net ERF$_{LU}$	LW'$_{CS}$	SW'$_{CS}$	LW CRE'	SW CRE'	NET'$_{CS}$	NET CRE'
UKESM1.0	$-0.17 \pm$ 0.04	$0.02 \pm$ 0.03	$-0.30 \pm$ 0.02	$0.03 \pm$ 0.01	$0.09 \pm$ 0.03	$-0.28 \pm$ 0.03	$0.11 \pm$ 0.03
UKESM1.1	$-0.21 \pm$ 0.04			Not available			
Standard	$-0.08 \pm$ 0.05	$0.02 \pm$ 0.02	$-0.19 \pm$ 0.03	$0.001 \pm$ 0.01	$0.09 \pm$ 0.03	$-0.17 \pm$ 0.04	$0.09 \pm$ 0.03
Complex	$-0.12 \pm$ 0.04	$0.00 \pm$ 0.02	$-0.20 \pm$ 0.02	$0.04 \pm$ 0.02	$0.05 \pm$ 0.03	$-0.20 \pm$ 0.03	$0.08 \pm$ 0.03

3.10 Comparison to other versions of UKESM (1.0 and standard 1.1)

Table 5 compares the land-use driven changes in TOA fluxes, excluding CH_4 and CO_2 impacts, for four model versions: the experimental set-up used here with both the standard and complex chemistry mechanisms, as well UKESM1.0 and UKESM1.1. This allows for an assessment of the impacts of process and parameter updates (section 2.1; Sands et al. (2025)). The net ERF$_{LU}$ is reduced for both chemistry mechanisms in the new model set-up. The new biosphere-atmosphere processes included in this research reduce ERF$_{LU}$ from -0.21 ± 0.04 W m^{-2} for UKESM1.1 to -0.08 ± 0.05 W m^{-2}. The impact of new process representation is smaller with the use of the complex chemistry mechanism, for which ERF$_{LU}$ is -0.12 ± 0.04 W m^{-2}. While the flux diagnostics for the Ghan (2013) method of decomposing the forcing were not available for UKESM1.1, a more detailed comparison can be made against UKESM1.0, for which ERF$_{LU}$ is also higher, with a magnitude of -0.17 ± 0.04 W m^{-2}.

We find the greatest change between model versions occurs for the clear-sky shortwave fluxes (SW'$_{CS}$ = IRF$_{ARI,SW}$ + Δ F$_{clear,clean,SW}$), which are expected to predominantly be driven by impacts from surface albedo changes and the aerosol-radiation interactions, alongside smaller effects from changes in greenhouse gases. Of all the separated fluxes, the SW'$_{CS}$ term has the greatest magnitude, regardless of model version. This is also the term that has changed most significantly between UKESM1.0 and the new simulations. SW'$_{CS}$ is of a much smaller magnitude in the updated model version (-0.19 ± 0.03 W m^{-2} and -0.20 ± 0.02 W m^{-2} for the standard and complex mechanisms) compared to UKESM1.0 (-0.30 ± 0.02 W m^{-2}). Both surface albedo, due to tuning the snow burial of vegetation, and sulphate aerosol representations have been adjusted between UKESM1.0 and UKESM1.1, which may drive some of the differences in SW'$_{CS}$ (Mulcahy et al., 2023). The new process representation included in the model simulations further changes the spatial distribution of BVOC emissions and the formation and growth of aerosols.

4 Discussion and conclusions

The contributions of O_3, ARI and the CRE to the pre-industrial to present-day land use change radiative forcing have been investigated in an updated configuration of the UK's Earth System Model from UKESM1.1. The net simulated ERF_{LU} (-0.08 ± 0.05 or -0.12 ± 0.04 W m^{-2} depending on the chemistry mechanism) is dominated by a negative forcing from changes in surface albedo. However, the positive IRF_{ARI} ($+0.06 \pm 0.02$ W m^{-2} or $+0.06 \pm 0.01$ W m^{-2}) and ΔCRE ($+0.09 \pm 0.03$ W m^{-2} or $+0.08 \pm 0.03$ W m^{-2}) offset a substantial part of this forcing. Separate calculations reveal changes in CH_4 lifetime as another negative forcing contribution, while increased CO_2 concentrations from land use carbon emissions have a positive forcing, leading to a total forcing (ERF_{LU} + ERF_{CH4} + RF_{CO2}) of +0.74 W m^{-2}. The net ERF_{LU} is similar to the estimates of Unger (2014a, b) (-0.11 ± 0.17 W m^{-2} and -0.17 W m^{-2}), while the total land use forcing inclusive of changes in CH_4 and CO_2 is within the uncertainty of the estimate of $+0.9 \pm 0.5$ W m^{-2} calculated by Ward et al. (2014), who also include CO_2 impacts. These results are also mostly consistent with existing land use radiative forcing studies in terms of the sign of the land use change forcing associated with particular pathways.

Changes in O_3 mixing ratios and CH_4 lifetime have a negative forcing, while aerosol effects, both direct and indirect, tend to have a positive forcing, as previously found by Unger (2014a, b); Heald and Geddes (2016); Scott et al. (2017). The O_3 forcing magnitude is in line with more recent experiments (e.g. Heald and Geddes, 2016; Scott et al., 2017), which suggest O_3 forcings of less than 0.03 W m^{-2}. To the best of our knowledge, this study is the first to find a potential change in stratospheric ozone from PI to PD land use change. The calculated CH_4 forcing is between that estimated by Scott et al. (2017) and Unger (2014a, b).

There are more differences compared with existing studies in the magnitude of the aerosol effects. Heald and Geddes (2016) show a negative forcing associated with an increase in nitrate aerosol, while all the aerosol forcings calculated here are positive. Nitrate aerosol is not included in the experimental setup used here, so the overall aerosol burden decreases and any increases due to agricultural emissions are not captured. Further, the indirect effects of aerosol calculated here are of a greater magnitude than those calculated by Scott et al. (2017). This may be due to Scott et al. (2017) using present-day conditions as the control, in which changes in biogenic aerosol have a much smaller impact relative to the total amount of aerosol compared with simulations using pre-industrial conditions. The sensitivity of aerosol effects to background conditions has been previously highlighted by Carslaw et al. (2017, 2013). In fact, an earlier study by Scott et al. (2014) highlights the sensitivity of the ΔCRE to background aerosol concentrations when testing the impacts of including organically mediated nucleation on BVOC radiative impacts.

From a process understanding perspective, the results can also be compared to other land cover or BVOC emission change experiments, even if they do not focus on pre-industrial to present-day transitions. The standard and complex chemistry mechanisms have recently been compared in experiments that quantified the effects of a two factor increase in BVOC emissions in UKESM1.0 under pre-industrial conditions (Weber et al., 2022). As found here, CH_4 responded more strongly to changes in BVOC emissions in the standard chemistry mechanism. The resulting radiative forcings tended to be of the opposite sign to the PI-to-PD land use forcing, consistent with the opposite directions of change in BVOC emissions. However, Weber et al. (2022)

found a positive ΔCRE when increasing BVOC emissions, while our results show a positive ΔCRE in response to reduced
BVOC emissions. The difference could be driven by the different spatial patterns of BVOC emission changes or the increased
hygroscopicity of organic aerosols and reduced hygroscopicity of sulphate aerosols in the new simulations. Weber et al. (2022)
attribute the positive ΔCRE to changes in sulphate aerosol driven by a reduction in OH. The change in process representation,
in particular increased OM hygroscopicity, may increase the relative role of organic aerosol compared with sulphate aerosol
in ACI. Previous research has found that CRE impacts can vary significantly depending on the treatment of BVOC and SOA
(Sporre et al., 2020).

Another UKESM1.1 study investigated the radiative effects of hypothetical future reforestation (Weber et al., 2024). Consistent with our results, the trace gas and surface albedo forcing act in the opposite direction to the aerosol direct effect. However,
the ΔCRE is found to be mostly statistically insignificant in that study. Further, Weber et al. (2024) find larger impacts from
O_3. Both of these differences could result from the more polluted atmosphere in present-day and future conditions compared to
the pre-industrial. Additionally, those experiments did not include the hygroscopicity updates, which may strengthen the sensitivity of the CRE to BVOC emissions. Overall, the forcings considered counteract up to 30% of the future land use change
CO_2 forcing in Weber et al. (2024), although this offsetting varied across different background climate scenarios, while the
results presented here show an offset of only around 15%. This highlights the relevance of the background conditions of the
atmosphere, in terms of both meteorology and chemical environment, the magnitude of the land use change and, potentially,
process representation for land use change impacts.

The impacts on atmospheric composition and the implications for radiative effects from land cover change of a very similar
magnitude (around -1000 Mha or -18%) are studied in present-day conditions using the EMAC model by Vella et al.
(2025a, b). While there are differences in the spatial patterns of the changes, global mean forcings from ARI and O_3 and CH_4
are of the same sign and similar magnitudes to those presented here. The key difference is, once again, in the magnitude and
sign of the ΔCRE, which is much smaller in the experiments conducted by Vella et al. (2025a). The present-day background
and the lack of new particle formation involving organic aerosol could diminish the impact of aerosol changes in the EMAC
experiments. Vella et al.'s present-day experiments are also nudged, which limits how much cloud properties, and subsequently
the CRE, can respond to perturbations in the model, as found by Collins et al. (2025).

Our results highlight the importance of including organically mediated boundary nucleation and up-to-date hygroscopicity
values within a model with interactive chemistry and aerosols to fully capture the aerosol forcings associated with land use
change. Aerosol forcing, in particular that from ACI, remains the largest source of uncertainty in the net PI to PD anthropogenic
radiative forcing (IPCC, 2021). Future UKESM experiments could expand this work further by including the nitrate scheme
(Jones et al., 2021) alongside interactive fire emissions (Teixeira et al., 2021) to incorporate changes in agricultural emissions
and biomass burning, closely linked to land use, in the net forcing. Particularly important to an improved understanding of
the overall forcing will be the use of emissions-driven models for CO_2 and CH_4, as has been suggested for future Coupled
Model Intercomparison Project phases (Sanderson et al., 2024). This will reduce the number of assumptions necessary when
calculating CO_2 and CH_4 forcings, as well as the assumptions of additivity and linearity when combining individual forcings,
and allow for interactions between all of the affected trace gases.

470 In conclusion, pre-industrial to present-day land use change in the UK's Earth System Model has a negative radiative forc-
ing, regardless of the chemistry mechanism used, when changes in CO_2 concentrations are excluded. Changes in atmospheric
composition and surface albedo mitigate around 15% of the positive forcing of land use carbon emissions. While the choice
of chemistry mechanism does not have a substantial impact on global mean forcing values, it drives significant regional dif-
ferences in, e.g., high-latitude stratospheric O_3 forcing. The sensitivity of atmospheric oxidation capacity to changes in BVOC

475 emissions is greater in the standard chemistry mechanism, which increases the magnitudes of the CH_4, O_3 and aerosol forc-
ings. Comparing the results presented here to existing studies highlights that the choice of pre-industrial background conditions
alongside updated process representation can increase the radiative forcing associated with changes in cloud properties. Land
use changes have significant impacts on atmospheric composition with substantial regional impacts on the radiative balance,
which may be even greater when re-evaluated in the future alongside additional processes such as agricultural emissions that

480 affect nitrate aerosol burdens. It is recommended that future land use simulations are run in an emissions-driven model for CO_2
and CH_4 to fully capture the interactions between vegetation and atmospheric trace gases and aerosols.

References

Archer-Nicholls, S., Abraham, N. L., Shin, Y. M., Weber, J., Russo, M. R., Lowe, D., Utembe, S. R., O'Connor, F. M., Kerridge, B., Latter, B., Siddans, R., Jenkin, M., Wild, O., and Archibald, A. T.: The Common Representative Intermediates Mechanism Version

495   2 in the United Kingdom Chemistry and Aerosols Model, Journal of Advances in Modeling Earth Systems, 13, e2020MS002 420, https://doi.org/https://doi.org/10.1029/2020MS002420, 2021.

Archibald, A. T., O'Connor, F. M., Abraham, N. L., Archer-Nicholls, S., Chipperfield, M. P., Dalvi, M., Folberth, G. A., Dennison, F., Dhomse, S. S., Griffiths, P. T., Hardacre, C., Hewitt, A. J., Hill, R. S., Johnson, C. E., Keeble, J., Köhler, M. O., Morgenstern, O., Mulcahy, J. P., Ordóñez, C., Pope, R. J., Rumbold, S. T., Russo, M. R., Savage, N. H., Sellar, A., Stringer, M., Turnock, S. T., Wild, O.,

500   and Zeng, G.: Description and evaluation of the UKCA stratosphere–troposphere chemistry scheme (StratTrop vn 1.0) implemented in UKESM1, Geoscientific Model Development, 13, 1223–1266, https://doi.org/10.5194/gmd-13-1223-2020, 2020.

Bennett, B. F., Salawitch, R. J., McBride, L. A., Hope, A. P., and Tribett, W. R.: Quantification of the Airborne Fraction of Atmospheric CO2 Reveals Stability in Global Carbon Sinks Over the Past Six Decades, Journal of Geophysical Research: Biogeosciences, 129, e2023JG007 760, https://doi.org/https://doi.org/10.1029/2023JG007760, _eprint:

505   https://agupubs.onlinelibrary.wiley.com/doi/pdf/10.1029/2023JG007760, 2024.

Canadell, J. G., Quéré, C. L., Raupach, M. R., Field, C. B., Buitenhuis, E. T., Ciais, P., Conway, T. J., Gillett, N. P., Houghton, R. A., and Marland, G.: Contributions to accelerating atmospheric CO_2 growth from economic activity, carbon intensity, and efficiency of natural sinks, Proceedings of the National Academy of Sciences, 104, 18 866–18 870, https://doi.org/10.1073/pnas.0702737104, _eprint: https://www.pnas.org/doi/pdf/10.1073/pnas.0702737104, 2007.

510   Carslaw, K. S., Lee, L. A., Reddington, C. L., Pringle, K. J., Rap, A., Forster, P. M., Mann, G. W., Spracklen, D. V., Woodhouse, M. T., Regayre, L. A., and Pierce, J. R.: Large contribution of natural aerosols to uncertainty in indirect forcing, Nature, 503, 67–71, https://doi.org/10.1038/nature12674, 2013.

Carslaw, K. S., Gordon, H., Hamilton, D. S., Johnson, J. S., Regayre, L. A., Yoshioka, M., and Pringle, K. J.: Aerosols in the Pre-industrial Atmosphere, Current Climate Change Reports, 3, 1–15, https://doi.org/10.1007/s40641-017-0061-2, 2017.

515   Chen, T., Rossow, W. B., and Zhang, Y.: Radiative Effects of Cloud-Type Variations, Journal of Climate, 13, 264 – 286, https://doi.org/10.1175/1520-0442(2000)013<0264:REOCTV>2.0.CO;2, place: Boston MA, USA Publisher: American Meteorological Society, 2000.

Collins, W. J., O'Connor, F. M., Byrom, R. E., Hodnebrog, Ø., Jöckel, P., Mertens, M., Myhre, G., Nützel, M., Olivié, D., Bieltvedt Skeie, R., Stecher, L., Horowitz, L. W., Naik, V., Faluvegi, G., Im, U., Murray, L. T., Shindell, D., Tsigaridis, K., Abraham, N. L., and Keeble,

520   J.: Climate forcing due to future ozone changes: an intercomparison of metrics and methods, Atmospheric Chemistry and Physics, 25, 9031–9060, https://doi.org/10.5194/acp-25-9031-2025, 2025.

Davin, E. L. and Noblet-Ducoudré, N. d.: Climatic Impact of Global-Scale Deforestation: Radiative versus Nonradiative Processes, Journal of Climate, 23, 97 – 112, https://doi.org/10.1175/2009JCLI3102.1, place: Boston MA, USA Publisher: American Meteorological Society, 2010.

525   Davin, E. L., de Noblet-Ducoudré, N., and Friedlingstein, P.: Impact of land cover change on surface climate: Relevance of the radiative forcing concept, Geophysical Research Letters, 34, https://doi.org/https://doi.org/10.1029/2007GL029678, _eprint: https://agupubs.onlinelibrary.wiley.com/doi/pdf/10.1029/2007GL029678, 2007.

Etminan, M., Myhre, G., Highwood, E. J., and Shine, K. P.: Radiative forcing of carbon dioxide, methane, and nitrous oxide: A significant revision of the methane radiative forcing, Geophysical Research Letters, 43, 12,614–12,623, https://doi.org/https://doi.org/10.1002/2016GL071930, _eprint: https://agupubs.onlinelibrary.wiley.com/doi/pdf/10.1002/2016GL071930, 2016.

Fiore, A. M., Dentener, F. J., Wild, O., Cuvelier, C., Schultz, M. G., Hess, P., Textor, C., Schulz, M., Doherty, R. M., Horowitz, L. W., MacKenzie, I. A., Sanderson, M. G., Shindell, D. T., Stevenson, D. S., Szopa, S., Van Dingenen, R., Zeng, G., Atherton, C., Bergmann, D., Bey, I., Carmichael, G., Collins, W. J., Duncan, B. N., Faluvegi, G., Folberth, G., Gauss, M., Gong, S., Hauglustaine, D., Holloway, T., Isaksen, I. S. A., Jacob, D. J., Jonson, J. E., Kaminski, J. W., Keating, T. J., Lupu, A., Marmer, E., Montanaro, V., Park, R. J., Pitari, G., Pringle, K. J., Pyle, J. A., Schroeder, S., Vivanco, M. G., Wind, P., Wojcik, G., Wu, S., and Zuber, A.: Multimodel estimates of intercontinental source-receptor relationships for ozone pollution, Journal of Geophysical Research: Atmospheres, 114, https://doi.org/https://doi.org/10.1029/2008JD010816, _eprint: https://agupubs.onlinelibrary.wiley.com/doi/pdf/10.1029/2008JD010816, 2009.

Fiore, A. M., Naik, V., Spracklen, D. V., Steiner, A., Unger, N., Prather, M., Bergmann, D., Cameron-Smith, P. J., Cionni, I., Collins, W. J., Dalsoren, S., Eyring, V., Folberth, G. A., Ginoux, P., Horowitz, L. W., Josse, B., Lamarque, J.-F., MacKenzie, I. A., Nagashima, T., O'Connor, F. M., Righi, M., Rumbold, S. T., Shindell, D. T., Skeie, R. B., Sudo, K., Szopa, S., Takemura, T., and Zeng, G.: Global air quality and climate, CHEMICAL SOCIETY REVIEWS, 41, 6663–6683, https://doi.org/10.1039/c2cs35095e, 2012.

Forster, P. M., Richardson, T., Maycock, A. C., Smith, C. J., Samset, B. H., Myhre, G., Andrews, T., Pincus, R., and Schulz, M.: Recommendations for diagnosing effective radiative forcing from climate models for CMIP6, Journal of Geophysical Research: Atmospheres, 121, 12,460–12,475, https://doi.org/https://doi.org/10.1002/2016JD025320, _eprint: https://agupubs.onlinelibrary.wiley.com/doi/pdf/10.1002/2016JD025320, 2016.

Ganzeveld, L., Bouwman, L., Stehfest, E., van Vuuren, D. P., Eickhout, B., and Lelieveld, J.: Impact of future land use and land cover changes on atmospheric chemistry-climate interactions, Journal of Geophysical Research: Atmospheres, 115, https://doi.org/10.1029/2010JD014041, publisher: John Wiley & Sons, Ltd, 2010.

Ghan, S. J.: Technical Note: Estimating aerosol effects on cloud radiative forcing, Atmospheric Chemistry and Physics, 13, 9971–9974, https://doi.org/10.5194/acp-13-9971-2013, 2013.

Guenther, A., Hewitt, C. N., Erickson, D., Fall, R., Geron, C., Graedel, T., Harley, P., Klinger, L., Lerdau, M., Mckay, W. A., Pierce, T., Scholes, B., Steinbrecher, R., Tallamraju, R., Taylor, J., and Zimmerman, P.: A global model of natural volatile organic compound emissions, Journal of Geophysical Research: Atmospheres, 100, 8873–8892, https://doi.org/10.1029/94JD02950, 1995.

Guenther, A. B., Jiang, X., Heald, C. L., Sakulyanontvittaya, T., Duhl, T., Emmons, L. K., and Wang, X.: The Model of Emissions of Gases and Aerosols from Nature version 2.1 (MEGAN2.1): an extended and updated framework for modeling biogenic emissions, Geoscientific Model Development, 5, 1471–1492, https://doi.org/10.5194/gmd-5-1471-2012, 2012.

Hantson, S., Knorr, W., Schurgers, G., Pugh, T. A., and Arneth, A.: Global isoprene and monoterpene emissions under changing climate, vegetation, CO 2 and land use, Atmospheric Environment, 155, 35–45, https://doi.org/10.1016/j.atmosenv.2017.02.010, 2017.

Heald, C. L. and Geddes, J. A.: The impact of historical land use change from 1850 to 2000 on secondary particulate matter and ozone, Atmospheric Chemistry and Physics, 16, 14 997–15 010, https://doi.org/10.5194/acp-16-14997-2016, 2016.

Heald, C. L. and Spracklen, D. V.: Land Use Change Impacts on Air Quality and Climate, Chemical Reviews, 115, 4476–4496, https://doi.org/10.1021/cr500446g, 2015.

565   Holmes, C. D.: Methane Feedback on Atmospheric Chemistry: Methods, Models, and Mechanisms, Journal of Advances in Modeling Earth
            Systems, 10, 1087–1099, https://doi.org/https://doi.org/10.1002/2017MS001196, 2018.

        IPCC: Summary for Policymakers, in: Climate Change and Land: an IPCC special report on climate change, desertification, land degrada-
            tion, sustainable land management, food security, and greenhouse gas fluxes in terrestrial ecosystems, edited by Shukla, P. R., Skea, J.,
            Calvo Buendita, V., Masson-Delmotte, H.-O., Pörtner, O., Roberts, D. C., Zhai, P., Slade, S., Connors, C., van Diemen, R., Ferrat, M.,
570   Haughey, E., Luz, S., Neogi, S., Pathak, M., Petzold, J., Portugal Pereira, J., Vyas, P., Huntley, E., Kissick, K., Belkacemi, M., and Malley,
            J., Cambridge University Press, 2019.

        IPCC: Climate Change 2021: The Physical Science Basis. Contribution of Working Group I to the Sixth Assessment Report of the Intergov-
            ernmental Panel on Climate Change, Tech. rep., IPCC, 2021.

        IPCC: The Earth's Energy Budget, Climate Feedbacks and Climate Sensitivity, in: Climate Change 2021 – The Physical Science Basis:
575   Working Group I Contribution to the Sixth Assessment Report of the Intergovernmental Panel on Climate Change, edited by Inter-
            governmental Panel on Climate Change (IPCC), pp. 923–1054, Cambridge University Press, Cambridge, ISBN 978-1-00-915788-9,
            https://doi.org/10.1017/9781009157896.009, 2023.

        Ito, A. and Hajima, T.: Biogeophysical and biogeochemical impacts of land-use change simulated by MIROC-ES2L, Progress in Earth and
            Planetary Science, Vol 7, Iss 1, Pp 1-15 (2020), https://doi.org/10.1186/s40645-020-00372-w, 2020.

580   Jones, A. C., Hill, A., Remy, S., Abraham, N. L., Dalvi, M., Hardacre, C., Hewitt, A. J., Johnson, B., Mulcahy, J. P., and Turnock, S. T.:
            Exploring the sensitivity of atmospheric nitrate concentrations to nitric acid uptake rate using the Met Office's Unified Model, Atmospheric
            Chemistry and Physics, 21, 15 901–15 927, https://doi.org/10.5194/acp-21-15901-2021, 2021.

        Jones, C. D., Arora, V., Friedlingstein, P., Bopp, L., Brovkin, V., Dunne, J., Graven, H., Hoffman, F., Ilyina, T., John, J. G.,
            Jung, M., Kawamiya, M., Koven, C., Pongratz, J., Raddatz, T., Randerson, J. T., and Zaehle, S.: C4MIP – The Coupled Cli-
585   mate–Carbon Cycle Model Intercomparison Project: experimental protocol for CMIP6, Geoscientific Model Development, 9, 2853–2880,
            https://doi.org/10.5194/gmd-9-2853-2016, 2016.

        Karset, I. H. H., Berntsen, T. K., Storelvmo, T., Alterskjær, K., Grini, A., Olivié, D., Kirkevåg, A., Seland, Ø., Iversen, T., and Schulz,
            M.: Strong impacts on aerosol indirect effects from historical oxidant changes, Atmospheric Chemistry and Physics, 18, 7669–7690,
            https://doi.org/10.5194/acp-18-7669-2018, 2018.

590   Mann, G. W., Carslaw, K. S., Spracklen, D. V., Ridley, D. A., Manktelow, P. T., Chipperfield, M. P., Pickering, S. J., and Johnson, C. E.:
            Description and evaluation of GLOMAP-mode: a modal global aerosol microphysics model for the UKCA composition-climate model,
            Geoscientific Model Development, 3, 519–551, https://doi.org/10.5194/gmd-3-519-2010, 2010.

        Morgenstern, O., Braesicke, P., O'Connor, F. M., Bushell, A. C., Johnson, C. E., Osprey, S. M., and Pyle, J. A.: Evaluation of the new UKCA
            climate-composition model - Part 1: The stratosphere, Geoscientific Model Development, 2, 43–57, https://doi.org/10.5194/gmd-2-43-
595   2009, 2009.

        Mulcahy, J. P., Johnson, C., Jones, C. G., Povey, A. C., Scott, C. E., Sellar, A., Turnock, S. T., Woodhouse, M. T., Abraham, N. L., Andrews,
            M. B., Bellouin, N., Browse, J., Carslaw, K. S., Dalvi, M., Folberth, G. A., Glover, M., Grosvenor, D. P., Hardacre, C., Hill, R., Johnson, B.,
            Jones, A., Kipling, Z., Mann, G., Mollard, J., O'Connor, F. M., Palmiéri, J., Reddington, C., Rumbold, S. T., Richardson, M., Schutgens,
            N. A. J., Stier, P., Stringer, M., Tang, Y., Walton, J., Woodward, S., and Yool, A.: Description and evaluation of aerosol in UKESM1
600   and HadGEM3-GC3.1 CMIP6 historical simulations, Geoscientific Model Development, 13, 6383–6423, https://doi.org/10.5194/gmd-
            13-6383-2020, 2020.

Mulcahy, J. P., Jones, C. G., Rumbold, S. T., Kuhlbrodt, T., Dittus, A. J., Blockley, E. W., Yool, A., Walton, J., Hardacre, C., Andrews, T., Bodas-Salcedo, A., Stringer, M., de Mora, L., Harris, P., Hill, R., Kelley, D., Robertson, E., and Tang, Y.: UKESM1.1: development and evaluation of an updated configuration of the UK Earth System Model, Geoscientific Model Development, 16, 1569–1600, https://doi.org/10.5194/gmd-16-1569-2023, 2023.

O'Connor, F. M., Boucher, O., Gedney, N., Jones, C. D., Folberth, G. A., Coppell, R., Friedlingstein, P., Collins, W. J., Chappellaz, J., Ridley, J., and Johnson, C. E.: Possible role of wetlands, permafrost, and methane hydrates in the methane cycle under future climate change: A review, Reviews of Geophysics, 48, https://doi.org/10.1029/2010RG000326, 2010.

O'Connor, F. M., Johnson, C. E., Morgenstern, O., Abraham, N. L., Braesicke, P., Dalvi, M., Folberth, G. A., Sanderson, M. G., Telford, P. J., Voulgarakis, A., Young, P. J., Zeng, G., Collins, W. J., and Pyle, J. A.: Evaluation of the new UKCA climate-composition model - Part 2: The Troposphere, Geoscientific Model Development, 7, 41–91, https://doi.org/10.5194/gmd-7-41-2014, 2014.

O'Connor, F. M., Abraham, N. L., Dalvi, M., Folberth, G. A., Griffiths, P. T., Hardacre, C., Johnson, B. T., Kahana, R., Keeble, J., Kim, B., Morgenstern, O., Mulcahy, J. P., Richardson, M., Robertson, E., Seo, J., Shim, S., Teixeira, J. C., Turnock, S. T., Williams, J., Wiltshire, A. J., Woodward, S., and Zeng, G.: Assessment of pre-industrial to present-day anthropogenic climate forcing in UKESM1, Atmospheric Chemistry and Physics, 21, 1211–1243, https://doi.org/10.5194/acp-21-1211-2021, 2021.

O'Connor, F. M., Johnson, B. T., Jamil, O., Andrews, T., Mulcahy, J. P., and Manners, J.: Apportionment of the Pre-Industrial to Present-Day Climate Forcing by Methane Using UKESM1: The Role of the Cloud Radiative Effect, Journal of Advances in Modeling Earth Systems, 14, e2022MS002 991, https://doi.org/https://doi.org/10.1029/2022MS002991, 2022.

Pacifico, F., Harrison, S. P., Jones, C. D., Arneth, A., Sitch, S., Weedon, G. P., Barkley, M. P., Palmer, P. I., Serça, D., Potosnak, M., Fu, T.-M., Goldstein, A., Bai, J., and Schurgers, G.: Evaluation of a photosynthesis-based biogenic isoprene emission scheme in JULES and simulation of isoprene emissions under present-day climate conditions, Atmospheric Chemistry and Physics, 11, 4371–4389, https://doi.org/10.5194/acp-11-4371-2011, 2011.

Pacifico, F., Folberth, G. A., Jones, C. D., Harrison, S. P., and Collins, W. J.: Sensitivity of biogenic isoprene emissions to past, present, and future environmental conditions and implications for atmospheric chemistry, Journal of Geophysical Research: Atmospheres, 117, https://doi.org/10.1029/2012JD018276, 2012.

Pincus, R., Forster, P. M., and Stevens, B.: The Radiative Forcing Model Intercomparison Project (RFMIP): experimental protocol for CMIP6, Geoscientific Model Development, 9, 3447–3460, https://doi.org/10.5194/gmd-9-3447-2016, 2016.

Prather, M. J.: Time scales in atmospheric chemistry: Theory, GWPs for CH4 and CO, and runaway growth, Geophysical Research Letters, 23, 2597–2600, https://doi.org/https://doi.org/10.1029/96GL02371, _eprint: https://agupubs.onlinelibrary.wiley.com/doi/pdf/10.1029/96GL02371, 1996.

Qu, X. and Hall, A.: Assessing snow albedo feedback in simulated climate change, Journal of Climate, 19, 2617–2630, 2006.

Rap, A., Scott, C., Spracklen, D., Bellouin, N., Forster, P., Carslaw, K., Schmidt, A., and Mann, G.: Natural aerosol direct and indirect radiative effects, Geophysical Research Letters, 40, 3297–3301, https://doi.org/10.1002/grl.50441, 2013.

Sanderson, B. M., Booth, B. B. B., Dunne, J., Eyring, V., Fisher, R. A., Friedlingstein, P., Gidden, M. J., Hajima, T., Jones, C. D., Jones, C. G., King, A., Koven, C. D., Lawrence, D. M., Lowe, J., Mengis, N., Peters, G. P., Rogelj, J., Smith, C., Snyder, A. C., Simpson, I. R., Swann, A. L. S., Tebaldi, C., Ilyina, T., Schleussner, C.-F., Séférian, R., Samset, B. H., van Vuuren, D., and Zaehle, S.: The need for carbon-emissions-driven climate projections in CMIP7, Geoscientific Model Development, 17, 8141–8172, https://doi.org/10.5194/gmd-17-8141-2024, 2024.

Sands, E., Doherty, R. M., O'Connor, F. M., Pope, R. J., Weber, J., and Grosvenor, D. P.: Biosphere–atmosphere related processes influence

640   trace-gas and aerosol satellite–model biases, Atmospheric Chemistry and Physics, 25, 7269–7297, https://doi.org/10.5194/acp-25-7269-2025, 2025.

Scott, C. E., Rap, A., Spracklen, D. V., Forster, P. M., Carslaw, K. S., Mann, G. W., Pringle, K. J., Kivekäs, N., Kulmala, M., Lihavainen, H., and Tunved, P.: The direct and indirect radiative effects of biogenic secondary organic aerosol, Atmospheric Chemistry and Physics, 14, 447–470, https://doi.org/10.5194/acp-14-447-2014, 2014.

645   Scott, C. E., Monks, S. A., Spracklen, D. V., Arnold, S. R., Forster, P. M., Rap, A., Carslaw, K. S., Chipperfield, M. P., Reddington, C. L. S., and Wilson, C.: Impact on short-lived climate forcers (SLCFs) from a realistic land-use change scenario via changes in biogenic emissions, Faraday Discussions, 200, 101–120, https://doi.org/10.1039/C7FD00028F, 2017.

Seinfeld, J. H. and Pandis, S. N.: Atmospheric Chemistry and Physics : From Air Pollution to Climate Change, John Wiley & Sons, Incorporated, https://ebookcentral.proquest.com/lib/ed/detail.action?docID=4462549, 2016.

650   Smith, C. J., Kramer, R. J., Myhre, G., Forster, P. M., Soden, B. J., Andrews, T., Boucher, O., Faluvegi, G., Fläschner, D., Hodnebrog, Ø., Kasoar, M., Kharin, V., Kirkevåg, A., Lamarque, J.-F., Mülmenstädt, J., Olivié, D., Richardson, T., Samset, B. H., Shindell, D., Stier, P., Takemura, T., Voulgarakis, A., and Watson-Parris, D.: Understanding Rapid Adjustments to Diverse Forcing Agents, Geophysical Research Letters, 45, 12,023–12,031, https://doi.org/https://doi.org/10.1029/2018GL079826, _eprint: https://agupubs.onlinelibrary.wiley.com/doi/pdf/10.1029/2018GL079826, 2018.

655   Sporre, M. K., Blichner, S. M., Schrödner, R., Karset, I. H. H., Berntsen, T. K., van Noije, T., Bergman, T., O'Donnell, D., and Makkonen, R.: Large difference in aerosol radiative effects from BVOC-SOA treatment in three Earth system models, Atmospheric Chemistry and Physics, 20, 8953–8973, https://doi.org/10.5194/acp-20-8953-2020, 2020.

Stevenson, D. S., Young, P. J., Naik, V., Lamarque, J.-F., Shindell, D. T., Voulgarakis, A., Skeie, R. B., Dalsoren, S. B., Myhre, G., Berntsen, T. K., Folberth, G. A., Rumbold, S. T., Collins, W. J., MacKenzie, I. A., Doherty, R. M., Zeng, G., van Noije, T. P. C., Strunk, A.,

660   Bergmann, D., Cameron-Smith, P., Plummer, D. A., Strode, S. A., Horowitz, L., Lee, Y. H., Szopa, S., Sudo, K., Nagashima, T., Josse, B., Cionni, I., Righi, M., Eyring, V., Conley, A., Bowman, K. W., Wild, O., and Archibald, A.: Tropospheric ozone changes, radiative forcing and attribution to emissions in the Atmospheric Chemistry and Climate Model Intercomparison Project (ACCMIP), Atmospheric Chemistry and Physics, 13, 3063–3085, https://doi.org/10.5194/acp-13-3063-2013, 2013.

Teixeira, J. C., Folberth, G. A., O'Connor, F. M., Unger, N., and Voulgarakis, A.: Coupling interactive fire with atmospheric composition and

665   climate in the UK Earth System Model, Geoscientific Model Development, 14, 6515–6539, https://doi.org/10.5194/gmd-14-6515-2021, 2021.

Thornhill, G., Collins, W., Olivié, D., Skeie, R. B., Archibald, A., Bauer, S., Checa-Garcia, R., Fiedler, S., Folberth, G., Gjermundsen, A., Horowitz, L., Lamarque, J.-F., Michou, M., Mulcahy, J., Nabat, P., Naik, V., O'Connor, F. M., Paulot, F., Schulz, M., Scott, C. E., Séférian, R., Smith, C., Takemura, T., Tilmes, S., Tsigaridis, K., and Weber, J.: Climate-driven chemistry and aerosol feedbacks in CMIP6 Earth

670   system models, Atmospheric Chemistry and Physics, 21, 1105–1126, https://doi.org/10.5194/acp-21-1105-2021, 2021a.

Thornhill, G. D., Collins, W. J., Kramer, R. J., Olivié, D., Skeie, R. B., O'Connor, F. M., Abraham, N. L., Checa-Garcia, R., Bauer, S. E., Deushi, M., Emmons, L. K., Forster, P. M., Horowitz, L. W., Johnson, B., Keeble, J., Lamarque, J.-F., Michou, M., Mills, M. J., Mulcahy, J. P., Myhre, G., Nabat, P., Naik, V., Oshima, N., Schulz, M., Smith, C. J., Takemura, T., Tilmes, S., Wu, T., Zeng, G., and Zhang, J.: Effective radiative forcing from emissions of reactive gases and aerosols – a multi-model comparison, Atmospheric Chemistry and

675   Physics, 21, 853–874, https://doi.org/10.5194/acp-21-853-2021, 2021b.

Twomey, S.: The Influence of Pollution on the Shortwave Albedo of Clouds, Journal of Atmospheric Sciences, 34, 1149 – 1152, https://doi.org/10.1175/1520-0469(1977)034<1149:TIOPOT>2.0.CO;2, place: Boston MA, USA Publisher: American Meteorological Society, 1977.

Unger, N.: Human land-use-driven reduction of forest volatiles cools global climate, Nature Climate Change, 4, 907–910, https://doi.org/10.1038/nclimate2347, 2014a.

Unger, N.: On the role of plant volatiles in anthropogenic global climate change, Geophysical Research Letters, 41, 8563–8569, https://doi.org/https://doi.org/10.1002/2014GL061616, _eprint: https://agupubs.onlinelibrary.wiley.com/doi/pdf/10.1002/2014GL061616, 2014b.

Vella, R., Forrest, M., Pozzer, A., Tsimpidi, A. P., Hickler, T., Lelieveld, J., and Tost, H.: Influence of land cover change on atmospheric organic gases, aerosols, and radiative effects, Atmospheric Chemistry and Physics, 25, 243–262, https://doi.org/10.5194/acp-25-243-2025, 2025a.

Vella, R., Gromov, S., Nussbaumer, C. M., Stecher, L., Kohl, M., Ruhl, S., Tost, H., Lelieveld, J., and Pozzer, A.: Shifts in global atmospheric oxidant chemistry from land cover change, EGUsphere, 2025, 1–29, https://doi.org/10.5194/egusphere-2025-1800, 2025b.

Voulgarakis, A., Naik, V., Lamarque, J.-F., Shindell, D. T., Young, P. J., Prather, M. J., Wild, O., Field, R. D., Bergmann, D., Cameron-Smith, P., Cionni, I., Collins, W. J., Dalsøren, S. B., Doherty, R. M., Eyring, V., Faluvegi, G., Folberth, G. A., Horowitz, L. W., Josse, B., MacKenzie, I. A., Nagashima, T., Plummer, D. A., Righi, M., Rumbold, S. T., Stevenson, D. S., Strode, S. A., Sudo, K., Szopa, S., and Zeng, G.: Analysis of present day and future OH and methane lifetime in the ACCMIP simulations, Atmospheric Chemistry and Physics, 13, 2563–2587, https://doi.org/10.5194/acp-13-2563-2013, 2013.

Walters, D., Baran, A. J., Boutle, I., Brooks, M., Earnshaw, P., Edwards, J., Furtado, K., Hill, P., Lock, A., Manners, J., Morcrette, C., Mulcahy, J., Sanchez, C., Smith, C., Stratton, R., Tennant, W., Tomassini, L., Van Weverberg, K., Vosper, S., Willett, M., Browse, J., Bushell, A., Carslaw, K., Dalvi, M., Essery, R., Gedney, N., Hardiman, S., Johnson, B., Johnson, C., Jones, A., Jones, C., Mann, G., Milton, S., Rumbold, H., Sellar, A., Ujiie, M., Whitall, M., Williams, K., and Zerroukat, M.: The Met Office Unified Model Global Atmosphere 7.0/7.1 and JULES Global Land 7.0 configurations, Geoscientific Model Development, 12, 1909–1963, https://doi.org/10.5194/gmd-12-1909-2019, 2019.

Wang, P., Holloway, T., Bindl, M., Harkey, M., and De Smedt, I.: Ambient Formaldehyde over the United States from Ground-Based (AQS) and Satellite (OMI) Observations, Remote Sensing, 14, https://doi.org/10.3390/rs14092191, 2022.

Ward, D. S., Mahowald, N. M., and Kloster, S.: Potential climate forcing of land use and land cover change, Atmospheric Chemistry and Physics, 14, 12 701–12 724, https://doi.org/10.5194/acp-14-12701-2014, 2014.

Weber, J., Archer-Nicholls, S., Abraham, N. L., Shin, Y. M., Bannan, T. J., Percival, C. J., Bacak, A., Artaxo, P., Jenkin, M., Khan, M. A. H., Shallcross, D. E., Schwantes, R. H., Williams, J., and Archibald, A. T.: Improvements to the representation of BVOC chemistry–climate interactions in UKCA (v11.5) with the CRI-Strat 2 mechanism: incorporation and evaluation, Geoscientific Model Development, 14, 5239–5268, https://doi.org/10.5194/gmd-14-5239-2021, 2021.

Weber, J., Archer-Nicholls, S., Abraham, N. L., Shin, Y. M., Griffiths, P., Grosvenor, D. P., Scott, C. E., and Archibald, A. T.: Chemistry-driven changes strongly influence climate forcing from vegetation emissions, Nature Communications, 13, 7202, https://doi.org/10.1038/s41467-022-34944-9, 2022.

Weber, J., King, J. A., Sindelarova, K., and Val Martin, M.: Updated isoprene and terpene emission factors for the Interactive BVOC (iBVOC) emission scheme in the United Kingdom Earth System Model (UKESM1.0), Geoscientific Model Development, 16, 3083–3101, https://doi.org/10.5194/gmd-16-3083-2023, 2023.

Weber, J., King, J. A., Abraham, N. L., Grosvenor, D. P., Smith, C. J., Shin, Y. M., Lawrence, P., Roe, S., Beerling, D. J., and Mar-
715   tin, M. V.: Chemistry-albedo feedbacks offset up to a third of forestation’s CO_2 removal benefits, Science, 383, 860–864,
https://doi.org/10.1126/science.adg6196, _eprint: https://www.science.org/doi/pdf/10.1126/science.adg6196, 2024.

Wu, S., Mickley, L. J., Kaplan, J. O., and Jacob, D. J.: Impacts of changes in land use and land cover on atmospheric chemistry and air quality
over the 21st century, Atmospheric Chemistry and Physics, 12, 1597–1609, https://doi.org/10.5194/acp-12-1597-2012, 2012.